Quantum Dot Interdiffusion For Two Colour Quantum Dot Infrared Photodetectors

Peter Kuffner

(u3289067)

Supervised by Dr Lan Fu & Prof Chennupati Jagadish

A thesis submitted as partial fulfillment of the requirements for the degree of Bachelor of Engineering with Honours at the Australian National University

April 2006

THE AUSTRALIAN
NATIONAL UNIVERSITY

Declaration

This thesis is an account of research undertaken under the supervision of Dr Lan Fu and Prof Chennupati Jagadish, between November 2004 and June 2005 in the quantum dot optoelectronic devices group at the Department of Electronic Materials Engineering, in the Research School of Physical Sciences and Engineering of the Australian National University. Except where acknowledged in the customary manner, the material presented in this thesis is my own work.

Peter Kuffner
11 April 2006

Acknowledgements

For the help and support I have received throughout the last year from a number of people, I am grateful.

I would like to thank my supervisors, Dr Lan Fu and Prof Chennupati Jagadish.

This project would not have been possible without Jagadish's guidance, enthusiasm, and encouragement. Thanks for planning a cool project and listening to my presentation so many times without showing boredom. I owe you for making sure others didn't monopolise equipment when I needed it.

Many, many, thanks go to Fu Lan, whose approachability and constant help was invaluable. Without your willingness to drop everything and answer my questions with the least warning, I would have learnt far less. I was told by many that I had an eye for detail before I met Fu, and now I know what a *real* eye for detail is.

Thanks to Hoe Tan and Michael Fraser ("*See* how cool nitrogen is!") for their help with the instruments in the lab and with LabView. You've got a vicious sense of humour, Hoe.

I would like to thank the whole group at EME for their random bits of help, particularly, Jenny Wong-Leung, Ian McKerracher, Kallista Stewart, and also Michael Gao for always helping me track down Fu Lan. I am thankful for the technical help that Tom Halstead provided, as well as his help in moving office so many times, and also for scabbing some good furniture for our office. The working environment at the research school was wonderful, with the great people at the school always giving interesting presentations (most of the time!) and holding plenty of functions with free food!

I owe a great deal to several people in the engineering department and within EME for their understanding and support during my long period of sickness. Thanks to Jagadish, Fu Lan, Hoe, Haley Jones, Adrian Lowe, and Pam Shakespeare.

My family deserve special thanks for all the support they have given me during this past year, and for tolerating my occasional totally-stressed-out behaviour. Thanks to mum and dad for helping me out during my long battle with eczema, and for your understanding. Much thanks goes to my little brother, for being inseparable. Adam, you truly are my trusty sidekick through thick and thin. Maximum respect, bro.

Finally, I'd like to thank Lee Sensei for his teachings all those years ago. The mastery of willpower in life was an important lesson, for it is through strength of mind that we realise the true strength of our bodies.

Abstract

An investigation into the effects of thermal interdiffusion on the characteristics of quantum dot infrared photodetectors (QDIPs) yields results useful for the creation of a two-colour QDIP. For high temperature rapid thermal annealing, quantum dot interdiffusion is induced, resulting in a large wavelength redshift in the photodetector spectral response, at the cost of a small degradation in device performance. The evaluation of a two-colour QDIP fabricated using selective suppression of interdiffusion during thermal annealing shows uniform performance in the two different detector pixels. This has implications as a useful process for the future fabrication of multi-colour QDIPs.

Publications

1. L. Fu, P. Kuffner, I. McKerracher, H. H. Tan, C. Jagadish, 'Rapid thermal annealing study of InGaAsGaAs quantum dot infrared photodetectors grown by metal organic chemical vapour deposition', *Proceedings of the 18th Annual Meeting of the IEEE Lasers and Electro-Optics Society, Sydney, Australia*, p. 228, (2005).

2. L. Fu, P. Kuffner, P. Gareso, H. H. Tan, C. Jagadish, 'Two-color InGaAs/GaAs quantum dot infrared photodetectors by controlled thermal interdiffusion', Submitted to Nanotechnology (2006).

Contents

List of Figures

Chapter 1

Introduction

1.1 Project Motivation

High performance infrared (IR) photodetection is desirable for many applications involving chemical analysis, night vision, thermal imaging, space ranging, remote sensing, mine detection and fibre-optic communications. Depending upon the application, one may desire either a broad, multicolour response from the detector, or a sharp single wavelength response. Multi-colour IR detection has the ability to determine the temperature of the observed body, in addition to producing images with some colour depth, so is much more favourable for a general imaging system. Multi-colour focal plane array (FPA) photodetectors are particularly useful for medical and military imaging as well as environmental monitoring applications.

Quantum dot infrared photodetectors (QDIPs) are part of a new breed of semiconductor nano-photonic devices, utilising stacked layers of quantum dots (QDs) as the active region in their structures. QD photodetectors are a promising new technology that will hopefully overcome many of the shortcomings of existing IR photodetection systems. QDIPs utilise inter-subband absorption to detect medium and long wavelength infrared radiation within the low absorption, 3-5μm & 8-14μm atmospheric 'windows'. There has been significant research into the study of QDIPs, but little in the way of multi-colour QDIP development, despite their desirability for a wide variety of applications.

Research in the fabrication of quantum dot devices is primarily focussed around the use of molecular beam epitaxy (MBE) to produce the QDs. Commercial production of semiconductors is, however, dominated by the use of metal-organic chemical vapour deposition (MOCVD). MOCVD has a greater volume scalability and much smaller production time for devices, but is more challenging to use for the formation of quantum dots. The integration of quantum dot devices into mainstream commercial applications hinges upon further research in producing quantum dot structures using MOCVD.

One of the aims of semiconductor device research is the production of photonic integrated circuits, such as logic devices and multicolour photodetector arrays. Tuning the operating wavelength of the active region differently for each device is necessary in order

to achieve this. Post-growth selective interdiffusion is a desirable method for this, because of its short processing time and cost effectiveness. Using dielectric capping, one can selectively suppress or promote interdiffusion in different pixels in a detector array, thereby making a multi-colour QDIP on a single wafer.

The aims of this project were to fabricate and characterise quantum dot infrared detectors grown using MOCVD, and then study the effects of quantum dot interdiffusion on QDIPs in order to test the feasibility of creating a two-colour detector. The research in this thesis is part of a larger effort to produce quantum dot nano-devices at the Electronic Materials Department, Research School of Physical Sciences and Engineering at the Australian National University. The ultimate aim of the photodetector research is to demonstrate high quality MOCVD grown single and multi-colour QDIPs.

1.2 Overview of this Thesis

The project undertaken for this thesis was split into two major parts. The first was a study into the effects of thermal interdiffusion on quantum dots, in order to gain an understanding necessary for the design of a two-colour QDIP. The second part was the fabrication and evaluation of a two-colour QDIP, using dielectric capping to selectively suppress interdiffusion in the quantum dot structure.

The following chapter sets out the background information necessary for an understanding of the project results. Chapter 3 details the experimental techniques used in the fabrication and analysis of all the QDIPs in this project. The results for the study of post-growth thermal interdiffusion on the performance of QDIPs are presented in Chapter 4. Chapter 5 describes the design of a two-colour quantum dot infrared photodetector fabricated using post-growth techniques, and presents the results from its characterisation. Finally, Chapter 6 presents the conclusions from the work undertaken for this thesis and some recommendations for future work.

Chapter 2

Background Theory

2.1 Overview of this Chapter

In this chapter, a discussion of the state of the art of semiconductor infrared photodetectors illuminates the significance of new quantum-dot-based devices. The nature of self-assembled quantum dots and their growth is then introduced, after which we present the details of quantum dot infrared photodetector structures and device operation. We follow this with the physics of quantum dot interdiffusion and the usefulness of thermal annealing as a method for creating a large redshift in the operating wavelength of QDIPs. Methods of enhancing and suppressing interdiffusion through the use of different dielectric capping layers are discussed in the final section.

2.2 Semiconductor Infrared Photodetectors

Max Planck first described the emission of electromagnetic (EM) radiation from bodies with the variation of temperature (Eisberg & Resnick 1974). Planck was made famous by the announcement of his spectral excitance law, which states how radiant heat transfer depends upon temperature (T) and wavelength (λ):

$$M(\lambda, T) = \frac{2\pi c}{\lambda^4 \left(e^{\frac{hc}{\lambda kT}} - 1\right)} \qquad \left(\frac{\text{Photons}}{cm^2 \cdot s \cdot \mu m}\right)$$

Where $c = 3 \times 10^8$m/s is the speed of light, $k = 5.67 \times 10^{-12}$Wcm^{-2}K^{-4} is the Boltzmann constant, and $h = 6.63 \times 10^{-34}$Js is Planck's constant.

A plot of Planck's law of spectral exitance shows that as the temperature of a blackbody increases, the wavelength of EM emission decreases (see figure 2.1). More interestingly, it shows that the majority of objects, those with a temperature 100K-400K, emit strongest of all in the infrared region of the electromagnetic spectrum. Additionally, the atmosphere has very low absorption in the medium and long wavelength, 3-5μm & 8-14μm ranges, making these the best wavelength ranges to spot extremely cold objects as well as everyday, room temperature, bodies. Since the 1940's, semiconductor infrared

photodetectors have been developed to take advantage of these physical facts (Saleh & Teich 1991).

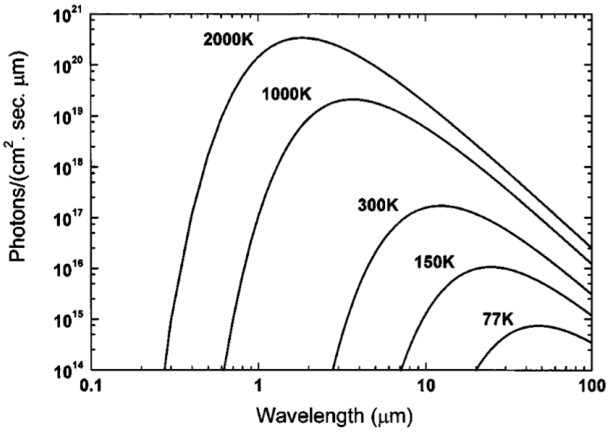

Figure 2.1: The spectral exitance from a blackbody at various tempertures, calculated using Planck's law.

Semiconductor IR detectors are required to have low dark current, high signal-to-noise ratio (detectivity) and low cost fabrication. There are three main types of semiconductor IR detectors, with their description based upon the type of transition used as the detection mechanism. InSb and mercury cadmium telluride (MCT) are intrinsic photodetectors (figure 2.2(a)), utilising an optical transition from the valence band to the conduction band as their mode of operation. A photon with an energy ($h\nu$) greater than the transition energy excites an electron from the valence band to the conduction band, creating free carriers which are then collected as photocurrent. Intrinsic detectors normally have narrow bandgaps, such as that of HgCdTe (MCT).

Doped semiconductors such as Si:In, Si:As, and Si:Ga are extrinsic detectors (figure 2.2(b)). They operate on the transition of an electron from the top of the impurity band to the conduction band, or, on the transition of a hole from the impurity band to the valence band. These detectors operate in the far infrared regime ($> 20\mu$m) and must operate at very low temperatures (liquid helium $\approx 2K$) with an impurity absorption that is limited by the substrate's impurity solubility.

Intersubband photodetectors are the third type to have been developed in the early 80's. The absorption mechanism is a transition between sub-levels of either the conduction or the valence band (2.2(c)). This type of transition requires the confinement of electrons in the active region through the use of different *heterostructures*. Heterostructures are semiconductor structures in which the composition changes with position, allowing the designer to modify the energy-band structure to control the motion of carriers within the semiconductor.

The quantum well infrared photodetector (QWIP), first proposed in 1977 (Esaki &

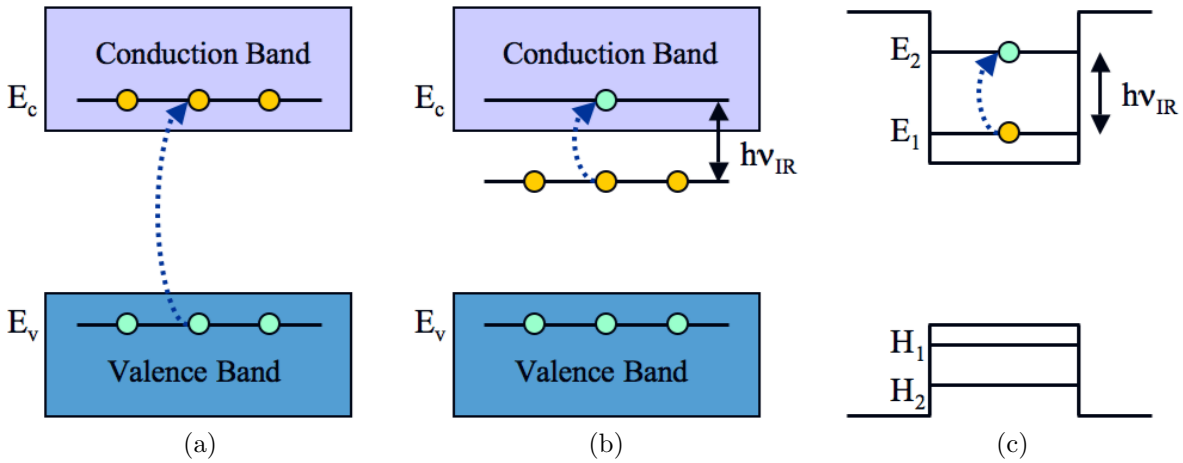

Figure 2.2: Band structure diagrams for the different semiconductor photodetectors. (a) Intrinsic absorption (HgCdTe; InSb). (b) Extrinsic absorption (Si:As; Si:P). (c) Intersubband absorption (QWIP; QDIP).

Sakaki 1977), is an intersubband detector that offers several advantages over the more common HgCdTe (MCT) photodetectors. QWIPs are made of the more significantly developed GaAs/$Al_xGa_{1-x}As$ materials, benefiting from the use of mature fabrication technologies. They are cheaper and easier to fabricate with a high uniformity across the surface of a wafer (Fu 2001). Low-cost fabrication of large, two-colour, 2-D focal plane arrays (FPA) have been demonstrated (Gunapala et al. 2000). QWIPs are not without their own problems, however. They have a low operating temperature, low absorption coefficient, and an inability to detect normally incident light, requiring the construction of special structures such as gratings and random reflectors on top of the devices (Sarusi et al. 1994).

Quantum dot infrared photodetectors (QDIPs) are a new type of intersubband detector made by replacing the quantum wells in QWIPs with quantum dots. QDIPs have unique properties originating from their three dimensional confinement of electrons, giving them a predicted superior performance over QWIPs (Ryzhii 1996, Liu et al. 2001, Stiff-Roberts et al. 2002). These include a low dark current and long carrier lifetime, leading to higher responsivity, detectivity and operating temperature. Operating temperatures as high as 250K have been reported (Tang et al. 2001). QDIPs do not suffer from the limitation in the incident photon polarisation due to selection rules that QWIPs must obey, and so are able to absorb normally incident light (Krishna et al. 2002). The development of commercially viable QDIPs hinges upon research into improving the quantum dot structures that they are based upon.

2.3 Self-Assembled Quantum Dots

The active region of QDIPs consists of stacked layers of quantum dots (QDs). Quantum dots are nano-scale strained island structures that form when a highly lattice mismatched ($> 1.8\%$) material is grown on a semiconductor substrate. In addition to photodetectors, devices such as lasers and amplifiers made using quantum dots have also been predicted to have higher performance than current technologies (Bimberg & Ribbat 2003). Due to their small size of 15-30nm and confinement in all three dimensions, quantum dots behave as 3D electron confinement 'boxes', with a discrete number of allowed energy states within them.

The confinement of carriers within a quantum dot leads to an atom-like density of states, and is the reason for the improvements in device performance. Figure 2.3 shows the density of states for different degrees of confinement in a semiconductor material. The density of states in a bulk material is a continuum that can be reduced with confinement in a quantum well (QW). Three dimensional confinement in a quantum dot reduces the density of states to a series of delta functions. If the energy levels in a QD are greater than kT apart, emission and absorption at a single wavelength is possible.

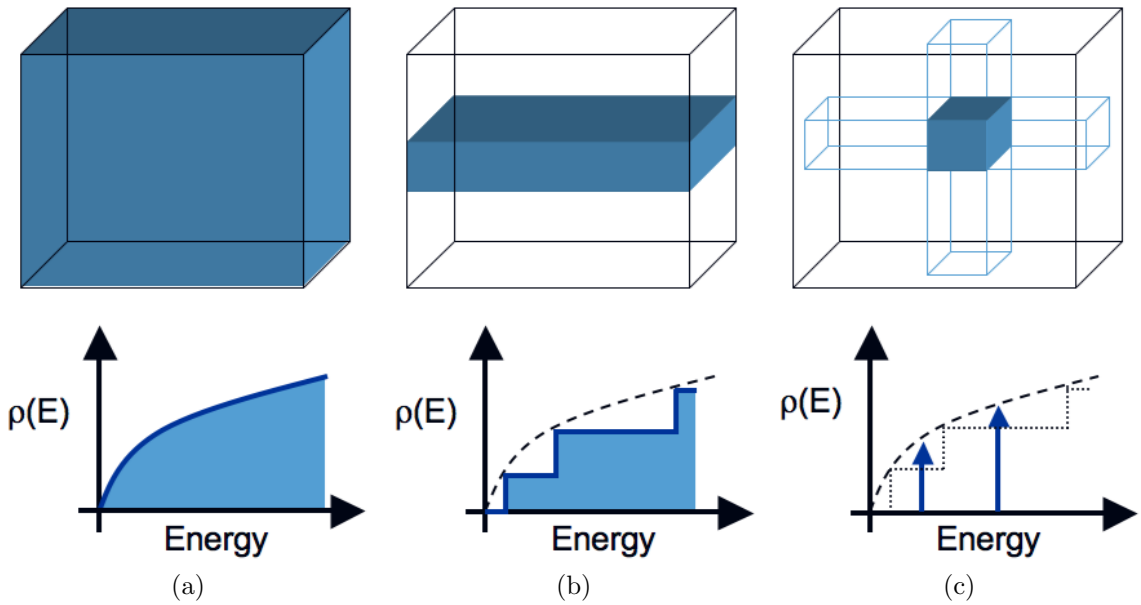

(a) (b) (c)

Figure 2.3: Schematic representation for the density of states for: (a) Bulk material, (b) 1D confinement within a quantum well (c) 3D confinement within a quantum dot.

Quantum dots were first made using e-beam lithography by patterning, etching and then regrowth. This method was impractical due to its time consuming nature and the defect and contamination issues associated with the etching and regrowth processes. The practicality of making semiconductor devices using quantum dots was realised with the discovery of the self-assembly growth technique in the 1980s (Goldstein et al. 1985).

Self-assmbled quantum dots are formed due to the strain difference between an epitaxially grown layer and its substrate. There are three forms of the epitaxial growth process that arise from the bonding energies, surface kinetics, and the difference in lattice constants of the materials used. All these are affected by the growth method and the choice of materials. Figure 2.4 shows the three different growth modes, starting with Frank van der Merwe growth in 2.4(a). This mode is layer-by-layer growth, where the materials have very little lattice mismatch and adatoms are more attracted to the surface due to low surface energy. The growth starts by a 2D nucleation process, where mono-layer (ML) islands are formed on the surface and expand outwards, completing each layer before forming the next. This can result in a series of flat layers, or a terraced structure if the substrate is not aligned to a crystal plane and adatoms attach preferentially to the edge of an existing layer. The opposite situation occurs in Volmer-Weber growth (figure 2.4(b)), where an extreme lattice mismatch exists. Large islands form directly on the surface because of the high surface energy and a low bond activation energy with atoms already deposited.

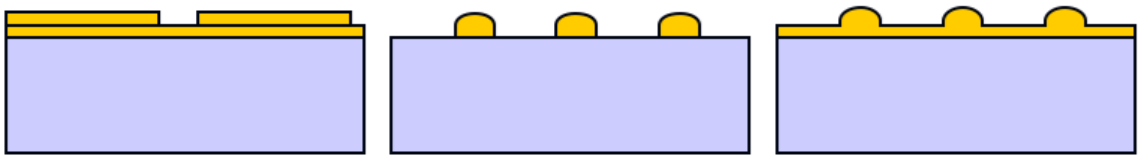

(a) (b) (c)

Figure 2.4: The different quantum dot growth modes: (a) Frank van der Merwe (layer-by-layer), (b) Volmer Weber (direct islanding), (c) Stranski-Krastanow.

The Stranski-Krastanow (SK) growth mode (figure 2.4(c)) is the intermediate case, where there is a moderate lattice mismatch in the materials. Self-assembled quantum dots are now almost exclusively grown in this mode. During this process, growth starts in the Frank van der Merwe mode (2D growth). As mono-layers of material are deposited, strain builds up linearly in the system due to the lattice mismatch, increasing the surface energy. At a critical thickness, called the 2D-3D growth transition, the deposition changes to islanding (3D growth) leading to a minimisation in the system's surface energy (Tersoff & LeGoues 1994) and a non-linear reduction in the strain with increasing deposition. For example, with $In_{0.5}Ga_{0.5}As$ quantum dots, the 2D-3D transition occurs at ≈4MLs of epitaxial growth in MBE (Leon & Fafard 1998) and at ≈6ML in MOCVD (Lever 2004). The layer immediately below the quantum dots is known as the wetting layer. The QD density and size distribution are both controlled by variation in the growth conditions and the choice of material.

The two main epitaxial methods used in the growth of self-assembled quantum dots are molecular beam epitaxy (MBE) and metal-organic chemical vapour deposition, MOCVD,

also known as metal-organic vapour phase epitaxy. The majority of QD research has been with the use of MBE due to built-in in-situ monitoring with reflection high energy electron diffraction (RHEED) systems. The low growth temperatures used in MBE also makes it easier to control the quantum dot growth. MOCVD is a much more favourable growth method in industry as its scalability makes mass production practical. High temperatures ($> 500°C$) inside MOCVD reactors are necessary in order for the source gases to crack efficiently, encouraging the clustering of atoms and the formation of defects. However, combined with the lack of mature in-situ monitoring in the system, control of QD growth with MOCVD is very difficult, requiring much research to optimise the growth conditions.

2.4 Quantum Dot Infrared Photodetectors

Quantum dot infrared photodetectors are advanced devices made from several stacked layers of quantum dots grown on a GaAs substrate. There are two basic device structures for intersubband QDIPs, described by the direction in which the photo-excited carriers move relative to the substrate plane. These are the vertical and lateral QDIP structures as shown in figures 2.5 and 2.6, respectively. In both structures, electrons are used as carriers due to their higher mobility. These structures are typically made from more than 5 layers of quantum dots, and QDIPs with up to 70 layers have been reported (Chakrabarti et al. 2004). Lateral QDIPs are believed to have the potential for better performance than vertical structures since the carriers have a higher mobility in the plane parallel to the quantum dot layers (Towe & Pan 2000). However, vertical QDIPs remain the most popular for research (Stiff et al. 2001, Stiff-Roberts et al. 2002), since the design is easier to fabricate into focal plane arrays (FPAs). As such, all the QDIPs in this work are a vertical detector structure.

Vertical QDIPs typically consist of an active region between heavily doped top and bottom contact layers grown on the GaAs substrate (Chen et al. 2001). The active region that is sensitive to IR radiation is made up of a stack of quantum dot layers, separated by GaAs barrier layers. The quantum dots themselves are typically InGaAs or InAs, and are sometimes Si (n^+) doped to increase the number of available carriers confined in the dots. The GaAs barrier layers separating the quantum dots are typically 30nm to 50nm thick. As a result, there is negligible vertical quantum-mechanical coupling between the dot layers, such that they are effectively independent in operation. Because of the strain built up in many layered structures, strain compensation layers can also be incorporated in the repeated structure (Lever et al. 2004*b*). The necessary metallisation deposited onto the Si doped top & bottom contacts finishes the device structure. The QDIP is in many ways just a complicated photosensitive resistor.

The band structure of an operating QDIP is shown in figure 2.7, where the detector

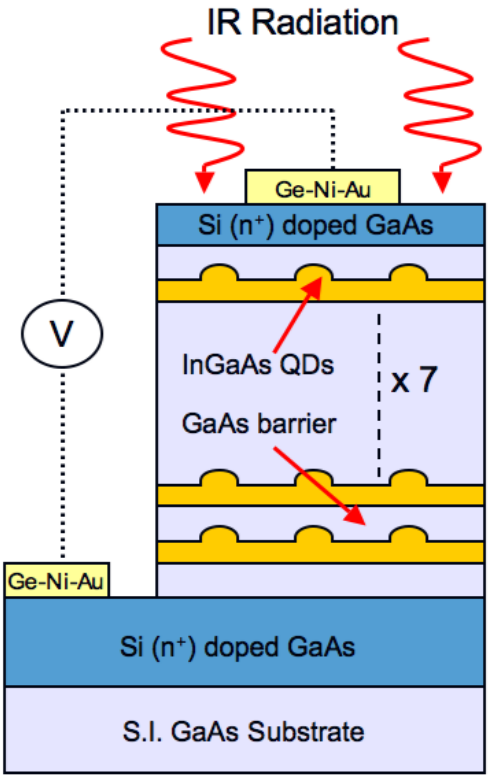

Figure 2.5: Cross-sectional schematic of a ten-layer vertical InGaAs/GaAs QDIP used in this thesis. Vertical transport of photo-excited carriers upwards through the QD layer stack brings them into the external circuit.

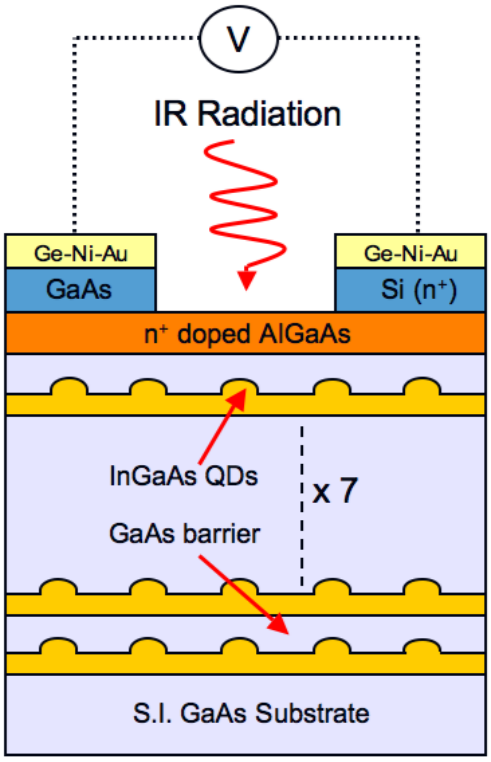

Figure 2.6: Cross-sectional schematic of a ten-layer lateral InGaAs/GaAs QDIP. Photo-excited carriers use lateral transport similar to that in a channel of a field effect transistor.

has a bias applied to its terminals. In this case the intersubband transition is taking place within the conduction band. Electrons confined within the dots are initially in the ground state. When the top of the detector is exposed to IR light, photons with an energy slightly greater than the intersubband transition energy excite carriers from the ground state of the confined potential to the excited state. Depending upon the position of the excited state, there are three transition modes for QDIPs: bound-to-bound, where the excited state is below the dot's barrier; bound-to-continuum, where the excited state is above the dot's barrier; or bound-to-quasi-continuum, as shown in figure 2.7.

Since the last decade, there has been extensive research on QDIPs (Xu et al. 1998, Pan et al. 1998, Phillips et al. 1999, Ye et al. 2002, Jiang et al. 2004). However, despite the high desirability for multi-colour IR detector systems, little has been done in multi-colour QDIP research. The development of multi-colour QDIPs requires the tuning of the detection wavelength through the design of the structure (either during growth or post-growth) or dynamically with the application of varying bias. Simultaneous multicolour detection within a single detector has been demonstrated (Krishna, Raghavan, von Winckel, Stintz,

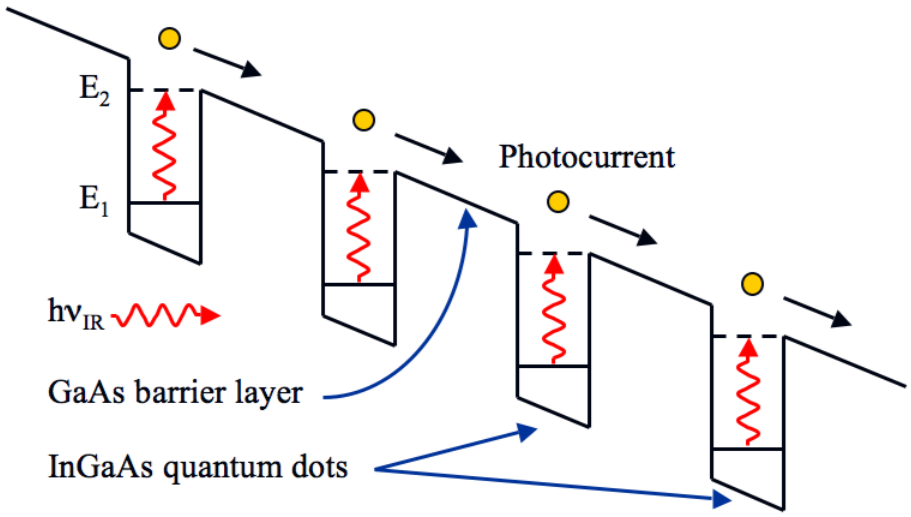

Figure 2.7: Schematic diagram of the conduction band of a QDIP operating under an electric field.

Ariyawansa, Matsik & Perera 2003). This multicolour absorption is due to the presence of multiple intersubband transitions in the active region based upon the size distribution of the quantum dots, which is extremely difficult to control and reproduce. While other voltage tuneable QDIPs have been reported (Kim & Harris 2004), most are simply a bias tuneable transition from one peak response to multiple colour response in a single pixel. Once again this behaviour is due of variation in dot size in the active region which is difficult to reproduce. For general imaging and temperature measurement purposes, one desires the bias tuneable response to switch between distinctly different colours, making these detectors less than ideal.

Recently, the dots-in-a-well (DWELL) QDIP design has been investigated (Raghavan et al. 2004). This is a new heterostructure where InAs dots are placed in an InGaAs well, the whole of which is placed within the usual top and bottom GaAs contact layers. Predicting the operational wavelength of a QDIP is difficult because of the sensitive self-assembled QD growth process. The DWELL structure demonstrates better control over the operational wavelength of the detector by varying the thickness of the well. Multi-colour DWELL detectors and a focal plane array have been made (Sakoglu et al. 2004, Krishna, Raghavan, von Winckel, Rotella, Stintz, Morath, Le & Kennerly 2003, Krishna et al. 2005), but there is considerable difficulty in making these structures since they require highly accurate and reproducible growth conditions. In this work, we demonstrate the simplicity, flexibility, and reproducibility of post-growth methods for tuning the wavelengths of QDIPs which makes them highly desirable for two-colour QDIP fabrication.

2.5 Thermal Interdiffusion of QDIPs for Wavelength Tuning

The thermal interdiffusion of quantum dots has been an important focus of research, with much work done on single and stacked QD layers. However, the effects of interdiffusion on full device structures have not been widely reported (Stewart et al. 2003, Hwang et al. 2005*a*).

There are several processes for inducing quantum dot intermixing (interdiffusion) in a QD structure. Interdiffusion can be initiated through annealing, ion implantation, or impurity induced intermixing processes. The simplest of these processes is rapid thermal annealing (RTA). Thermal annealing has been demonstrated to be able to induce a large wavelength shift in the quantum dots without any damage to the structure that other methods may cause.

Thermal interdiffusion in III-V compound semiconductors is primarily driven by the diffusion of point defects such as vacancies and interstitials. Diffusion occurs along concentration gradients in the dot layers, in the same way as for quantum wells (Lever 2004), causing the interfaces between dots and barriers to become interdiffused. This alters the potential profile of each quantum dot, changing the transition energy and leading to a redshift in the dot's absorption wavelength, as well as a blueshift in photoluminescence spectra (Leon et al. 1996, Lever et al. 2003), as shown in figure 2.8. With the change in the transition states, the height of the dot's barrier is effectively smaller, and the modified separation of the confined states results in the wavelength shifts.

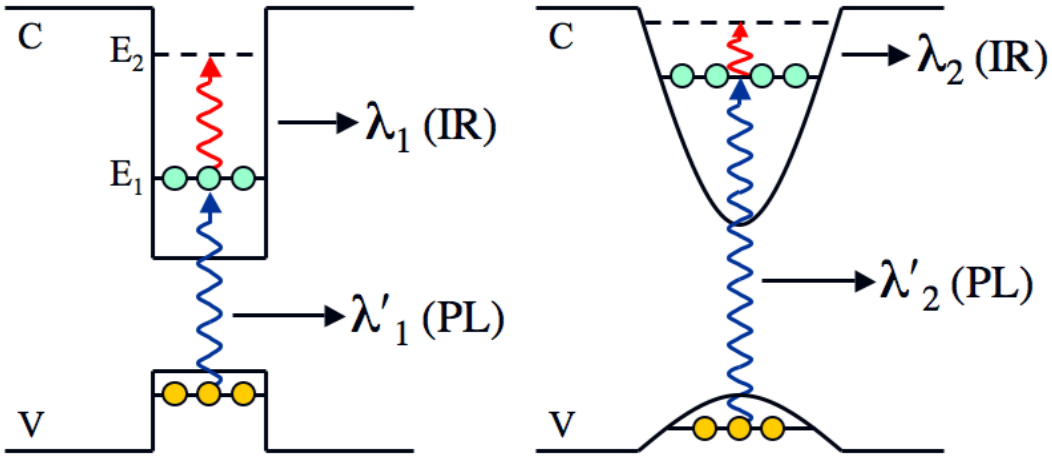

Figure 2.8: The energy profile of a quantum dot before and after interdiffusion. The infrared (IR) absorption photon, λ_2, has a longer wavelength than that of λ_1. In photoluminescence (PL) emission, photon λ_2' has a shorter wavelength than that of λ_1'

Quantum dots are highly compressively strained structures, with a 3D shape that also

gives them a very large surface-area-to-volume ratio. The high Indium concentration in quantum dots creates a large concentration gradient. These reasons mean that quantum dots are susceptible to a large amount of interdiffusion. The amount of interdiffusion is dependent on the annealing temperature, and also the duration of annealing. The growth conditions and type of structure also influence the interdiffusion, since the grown-in defects in the structure and the Indium composition play an important part in the process. Extremely high annealing temperatures can also have a negative effect, as the quantum dots may diffuse too much and become 2D structures, changing their characteristics heavily. Additionally, stacked QD structures have an upper limit. If the temperature of the annealing is too high, there is the possibility that strain relaxation can take place in the structure, causing the formation of extended defects that degrade the QD properties.

2.6 Promotion and Suppression of Interdiffusion Using Dielectric Capping

Although thermal interdiffusion is very simple and effective, by itself it does not have selectivity. There are several different ways of achieving selective, controllable interdiffusion in QD structures. Impurity induced intermixing, ion implantation induced intermixing and impurity free vacancy disordering (IFVD) are all well known methods for achieving selective intermixing. IFVD is the simplest of these methods and the one most suitable for device fabrication since it does not introduce any additional impurities into the sample.

IFVD involves depositing a layer of dielectric film onto the top of the sample before thermal annealing. SiO_2 is the most common capping layer, responsible for the promotion of interdiffusion in quantum well and quantum dot layers. The opposite of IFVD is also possible with a dielectric capping technique, where thermal interdiffusion can be largely suppressed when the QD structure is capped with TiO_2 (Lever et al. 2004*a*).

The mechanism for IFVD in III-V semiconductors is the generation and diffusion of Ga vacancies within the structure. Ga diffusion out of the top GaAs layer of the structure and into the dielectric capping layer creates additional Ga vacancies. These vacancies then diffuse down through the structure, enhancing the interdiffusion process. The amount of additional diffusion that occurs is controlled by the type of dielectric material and the thickness of the deposited layer. This is because the solubility of Ga in the capping layer determines the amount of Ga atoms that the layer can absorb. The type of capping material has an additional important effect, since it's thermal expansion coefficient (α) will be different to that of the GaAs layer. This mismatch in α creates stress in the GaAs during annealing. Figure 2.9 shows the different thermal stress effects of SiO_2 capping, and TiO_2 capping during the annealing process.

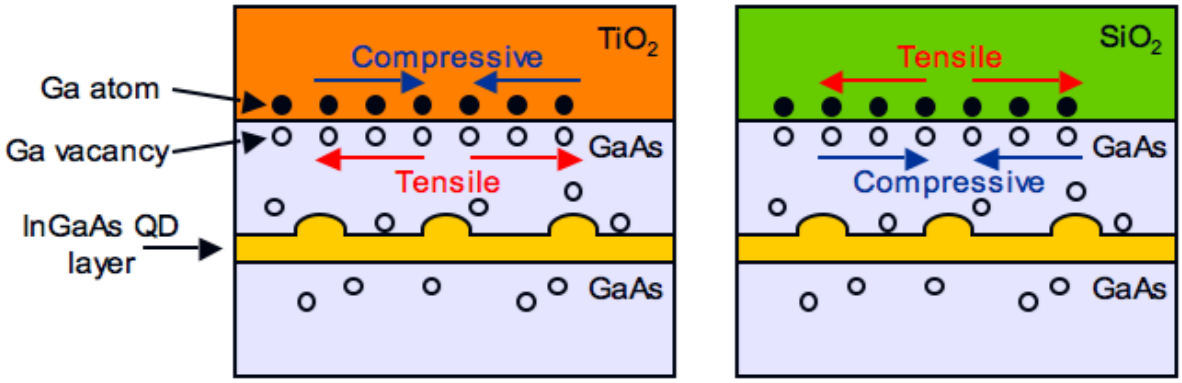

Figure 2.9: Thermal stress effects of TiO_2 and SiO_2 capping during annealing of a QD structure. During annealing, TiO_2 creates tensile stress on the GaAs that inhibits Ga vacancy diffusion, while IFVD with SiO_2 does the opposite, enhancing interdiffusion.

When TiO_2 is used, which has a larger thermal expansion coefficient than that of GaAs ($\alpha_{TiO_2} = 8.19 \times 10^{-6}\ ^\circ C^{-1}$ & $\alpha_{GaAs} = 6.86 \times 10^{-6}\ ^\circ C^{-1}$), tensile stress will be created in the GaAs to trap the Ga vacancies within the QD structure, inhibiting interdiffusion. On the other hand, if SiO_2 is deposited on the quantum dot structure, the high Ga solubility of SiO_2 also enables the creation of more Ga vacancies in the QD structure. The smaller thermal expansion coefficient of SiO_2 ($\alpha_{SiO_2} = 0.52 \times 10^{-6}\ ^\circ C^{-1}$), relative to the GaAs results in the application of compressive strain to the QD structure, enhancing the mobility of Ga vacancies, making SiO_2 highly desirable for increasing the interdiffusion effect.

Furthermore, it has also been found that the use of a bi-layer TiO_2/SiO_2 capping layer results in the suppression of interdiffusion (Fu et al. 2003). In this case, TiO_2 is deposited over the top of a thin SiO_2 layer. The promotion of interdiffusion from IFVD with the SiO_2 is suppressed by the large strain from the TiO_2 during annealing, provided that the SiO_2 layer is relatively thin. This bi-layer structure is important for fabrication purposes, as the removal of the TiO_2 after the annealing is made easier by etching the underlying layer of SiO_2 using wet chemical etching. This wet etching removal makes the use of TiO_2 as a capping layer to suppress interdiffusion and IFVD a simple and attractive process.

Chapter 3

Experimental Methodology

3.1 Overview of this Chapter

In this chapter the experimental techniques used in this study are presented. We begin with the details of the epitaxial growth of the QDIP structure, and then the methods used for dielectric capping of samples. The post-growth annealing process that is responsible for initiating interdiffusion of the QDIP samples is described. It is followed by the methodology for the different processing techniques involved in the fabrication of QDIPs. Finally, the main photodetector characterisation techniques are described.

3.2 MOCVD Growth of the Quantum Dot Structure

The QD structure used to make the detectors in this thesis consisted of stacked layers of quantum dots grown by metal-organic chemical vapour deposition (MOCVD) on a single wafer. The growth of the structure was performed by Dr Lan Fu using EME's MOCVD reactor, in the time just prior to the commencement of my project. Due to the difficulty inherent in the growth of quantum dots, the critical parameters such as growth temperature, growth rate and V/III ratio had been optimised for the 10-layer structure to obtain good quality QD layers with high dot density and uniformity.

Metal-organic chemical vapour deposition is a process wherein a volatile metal-organic vapour mixture is passed over a heated substrate to epitaxially grow crystals. Ultra-high purity H_2 is used as a carrier gas, passing through bubblers containing the group III precursors trimethylgallium (TMGa) and trimethylindium (TMIn) to obtain the gallium and indium. The gaseous group V precursor arsine (AsH3) supplies arsenic. Silane (SiH_4) is used to supply the silicon for n-type doping. The reactor is kept at low pressure (100mbar) with the wafer placed on a rotating graphite susceptor and heated by infrared lamps. The source gases entering the heated chamber decompose into radicals and react at the surface of the wafer. Growth is controlled by temperature, duration, and the amount of group V relative to group III material supplied (V/III ratio).

The QDIP structure is shown in figure 3.1, and is an n-i-n structure grown on a

semi-insulating GaAs (001) substrate. The structure contained 10 layers of undoped $In_{0.5}Ga_{0.5}As$ QDs, each a thickness of 5.7 atomic monolayers (ML). The quantum dot layers were each separated with $50nm$ GaAs barrier layers, with the whole stack sandwiched between two highly Si-doped ($n^+ \approx 2 \sim 3 \times 10^{18} cm^{-3}$) top (300nm) and bottom (1000nm) GaAs contact layers.

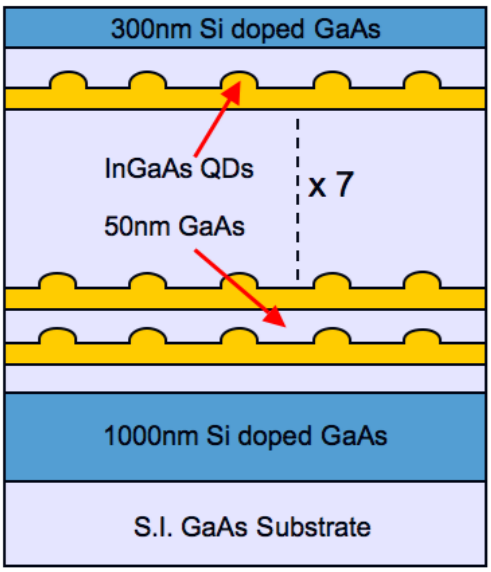

Figure 3.1: Cross-sectional schematic of the ten-layer InGaAs/GaAs QDIP structure used in this thesis.

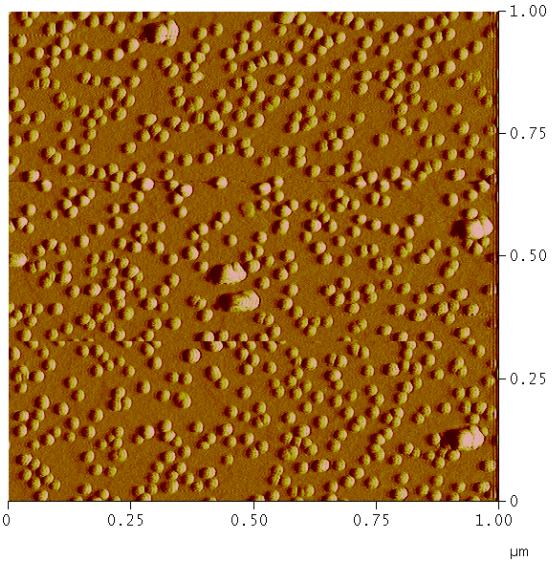

Figure 3.2: AFM image of the topmost QD layer of the un-capped ten-layer stacked structure.

The n-type GaAs contact layers were grown at 650°C with V/III ratio of 69 and growth rate of 2.3 ML/s. The QDs and GaAs spacer layers were grown at 550°C. The QDs were formed by depositing InGaAs at a rate of 1.7 ML/s and a V/III ratio of 15. The GaAs barrier layers were deposited at 2.3 ML/s. After capping the QDs with the first 7nm GaAs (at a V/III ratio of 15), the growth was interrupted to increase the V/III ratio to 40 to grow the remainder 43nm of the GaAs. These conditions were chosen in order to planarise the GaAs surface for the next QD layer growth. Once the stacked layers of quantum dots had been grown, the structure was separated into small samples using a diamond tip.

A second identical ten-layer stack QD structure was also grown under the same conditions but the growth was stopped after the 10th QD layer, leaving the quantum dots uncapped for an atomic force microscopy (AFM) measurement. The AFM results in figure 3.2, show that the dot density was $6 \times 10^{10} cm^{-2}$ with an average height and width of 3.1 nm and 18.9 nm, respectively.

3.3 Dielectric Capping Using PECVD and E-beam

Deposition of SiO_2 and TiO_2 dielectric layers was performed on one of the samples prior to annealing in order to suppress interdiffusion to create a two-colour QDIP. SiO_2 was deposited on the sample first, while TiO_2 was deposited over the top of the SiO_2 layer.

Plasma enhanced chemical vapour deposition (PECVD) was used for the deposition of the SiO_2 layer. The PECVD system creates a partially ionised gas between two electrodes, one of which is grounded and has the sample placed upon it. The plasma is created by application of an RF field to the gas, accelerating electrons and creating an ionisation cascade as electrons collide with atoms in steady state operation. A fraction of the ions in the plasma undergo excitation into reactive species and diffuse down to the sample, reacting with the surface to form a solid film over time. A 5% concentration of SiH_4 in N_2 and N_2O was used as the source gas mixture for the SiO_2 deposition, in which 10∼15nm of SiO_2 were deposited.

The TiO_2 deposition was done using electron-beam (e-beam) evaporation. In this process, the material to be deposited is heated by a focussed electron beam, causing the material to evaporate from the small focal area to deposit on the sample. The thickness of the evaporated TiO_2 layer was 180nm.

The TiO_2/SiO_2 capped sample underwent thermal annealing as described below. The bi-layer capping was then removed using a 20% mixture of HF acid and water, prior to device fabrication.

3.4 Post-Growth Rapid Thermal Annealing

In order to initiate interdiffusion in the QDIP structures, thermal annealing is necessary. The QDIP samples were put through a post-growth annealing process using the EME rapid thermal annealing (RTA) furnace for 30s each at different temperatures. For the thermal interdiffusion study these were: 600°C, 650°C, 700°C, 750°C, and 800°C. For the creation of the two-colour detector, the annealing temperature was 750°C. All the anneals were carried out under Ar ambient with the temperature ramped up at 100°C/s. During annealing, the QDIP samples were sandwiched between two additional pieces of GaAs to prevent As desorption which occurs at temperatures above 400°C. After annealing the samples were allowed to cool down naturally under the ambient Ar gas. A single sample, known as the as-grown sample, was kept un-annealed in order to act as the reference sample for the study.

3.5 QDIP Device Fabrication

Several standard semiconductor processing methods were necessary to fabricate the infrared photodetectors from the annealed samples. All the samples in this work were fabricated into QDIPs with the methodology detailed in the two distinct stages below.

3.5.1 Cleaning and Mesa Structure Definition

The first stage was to define the mesa structure for the QDIPs using standard photolithography and wet chemical etching techniques. The following steps were carried out for each sample:

1. Cleaning using warm trichloroethylene (TCE), ultrasonic cleaning with acetone and ethanol, and with a final rinse in D.I. water.

2. Heating of the sample in an oven at 85°C for 5 minutes, to remove residual solvent.

3. Spin-on of the photoresist at a speed of 4000rpm for 30s.

4. Soft baking of the sample in an oven at 85°C for 15 minutes.

5. Photolithography by masking of the sample and exposure to focussed light from a mercury vapour lamp for 25s.

6. Development of the sample in a solution with a 2:1 ratio of developer to H_2O for 20s. This process left a pattern of two rows of 250μm×250μm photoresist squares on the sample (figure 3.3(a)), in order to make multiple QDIPs on each sample.

7. Hard baking of the patterned sample in an oven for 2 minutes at 120°C to harden the photoresist in preparation for etching.

8. The use of wet chemical etching to etch away the unmasked area of the sample down to the depth of the Si-doped GaAs bottom contact layer, defining the mesa structures. The chemical mixture consisted of 1:1:3 H_3PO_4:H_2O_2:H_2O cooled to 4°C to slow the reaction time in order to control the etch depth precisely.

9. Removal of the photoresist using acetone.

Figures 3.3(b)-(d) show the cross-section of single mesa formed using these processing steps.

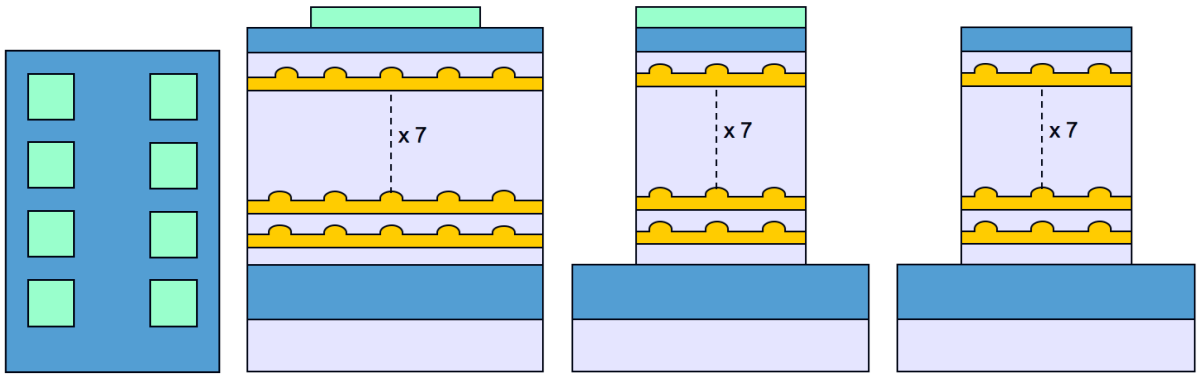

Figure 3.3: Schematic of the mesa structure formation process. Photoresist is shown in pale green in all pictures. (a) The top-down view of a patterned sample, with the photoresist marked in green. (b) The sample cross-section with a photoresist square on top. (c) Cross-section after wet chemical etching. (d) A single mesa cross-section after photoresist removal.

3.5.2 Metal Contact Formation and Packaging

The second stage was the formation of the metal contacts and the final packaging. A second photolithography step was carried out to define areas for the metal contacts on the QDIPs. The lithography procedure described in the processing step above was repeated using a different mask. The pattern for the contacts consisted of leaving clear circles of 150μm diameter on top of each mesa and long clear rails on the bottom contact layer, with the rest of the sample covered in photoresist (figure 3.4(a)). In this way, each QDIP on a sample would have an independent top contact and a shared bottom contact.

After the second photolithography step, metal contacts were formed using the following steps:

1. The removal of natural oxidation by dipping the sample in 10% HCl for 40s.

2. The use of e-beam evaporation to deposit layers of germanium, nickel and gold for the n-type metal contacts. Each metal was successively evaporated onto the sample with the following thicknesses: 20nm Ge, 15nm Ni, 200nm Au.

3. Metal lift-off using acetone to lift off the metal-covered photoresist from the rest of the surface of the sample.

4. Metal contact alloying for 60s at a temperature of 380°C.

Figures 3.4(b)-(d) show a single QDIP formed from this metallisation process.

The finished device was finally packaged by mounting it in a 14-pin chip-carrier, as shown in figure 3.5(a). 25μm thick gold wires were bonded to the metal contacts on all

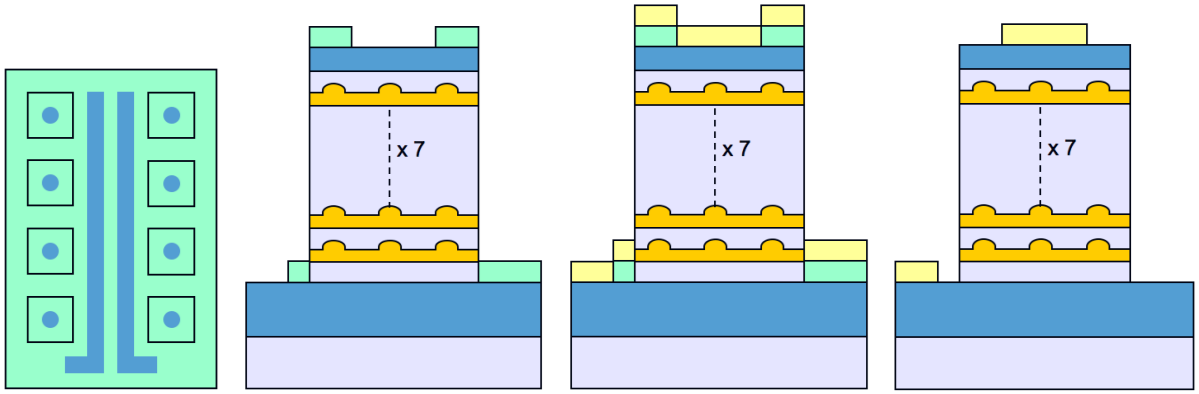

Figure 3.4: Schematic of the metallisation process. Photoresist is shown in pale green, and metal is shown in pale yellow in all pictures. (a) The top-down view of a patterned sample, with the photoresist marked in green. (b) A mesa cross-section with areas on the contact layers clear of the photoresist. (c) Cross-section after metal deposition. (d) A single QDIP cross-section after final metal lift-off.

the QDIPs in the sample, connecting them to the gold pins on the package. The upper contacts were all wired to individual pins on the chip-carrier, while the bottom contact rail was wired into a single common pin. Figure 3.5(b) shows a microscope image of the surface of a completed QDIP sample.

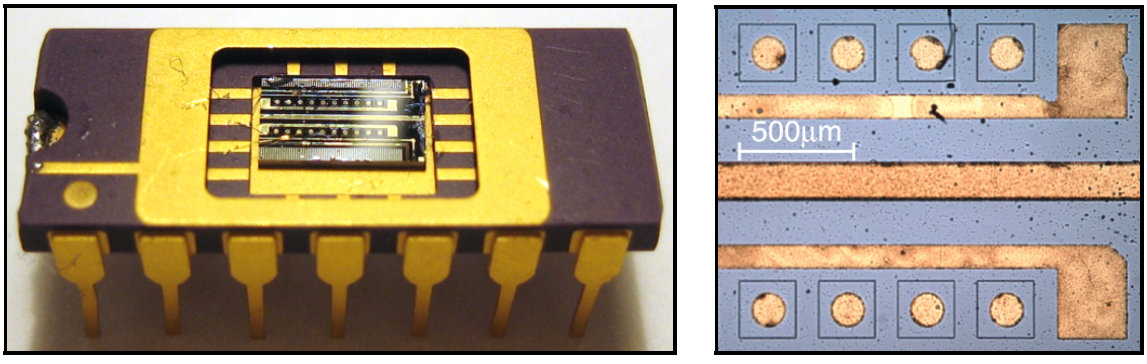

Figure 3.5: Photographs of a completed QDIP sample. (a) The QDIP array mounted in a 14-pin chip-carrier and wired up. (b) Microscope image of the surface of the QDIP array, showing the unwired pixels. A small amount of dirt has accumulated on the surface during measurements.

3.6 QDIP Characterisation

An infrared photodetector is characterised by several important parameters. These are the spectral response, peak responsivity, specific detectivity, and the dark current den-

sity. Determination of these parameters requires the measurement of the QDIP spectral response, calibrated IR signal response, noise current, and dark current I-V characteristic.

3.6.1 Spectral Response

The spectral response characterises a photodetectors operational wavelength range. The spectral response is an important characteristic that determines the applications for which the detector can be used due to its peak wavelength and the spectral width. The normalised spectral response for each sample was obtained using a Fourier transform infrared spectrometer (FTIR). An evenly stepped bias was applied to each QDIP with the spectral response measured at each step.

In order to take the measurement, a QDIP sample (wired to a chip carrier) was mounted inside a liquid Nitrogen cooled cryostat, maintaining its temperature at 77K. The base of the chip-carrier was bonded with silver paste to the mount in the cryostat, and the chip-carrier's pins were soldered to wires connected to the cryostat's output pins. BaF_2 was used as the window material on the cryostat since it does not absorb any infrared radiation at wavelengths below 12μm. This material made the window transparent to the section of the spectrum that was of interest in this measurement, namely the wavelength range for typical QDIPs.

The spectral response measurement was then made using a Nicolet Impact Bench 400 FTIR spectrometer as shown in figure 3.6. A device from the QDIP sample was used as the detector in the measurement, replacing the FTIR systems DTGS detector. QDIPs have a low photocurrent signal, so the output signal from the QDIP was received by the SRS-570 low noise current preamplifier. The preamplifier was additionally used to provide the bias control for the QDIP, with voltage readings taken using a multimeter.

3.6.2 Peak Responsivity

The responsivity of a detector is the signal output normalised by the radiant power input. The absolute peak responsivity is given by using the integrated incident power over all wavelengths for the radiant power input:

$$R_{peak} = \frac{I_{signal}}{A\int_0^\infty R'(\lambda)Q(\lambda)d\lambda} \tag{3.1}$$

Where the peak responsivity, R_{peak}, has units of Amps/Watt. A is the area of the detector, I_{signal} is the photocurrent, $R'(\lambda)$ is the normalised responsivity, and $Q(\lambda)$ is the radiant power input, or incidance.

The peak responsivity is determined through two measurements. The first is the

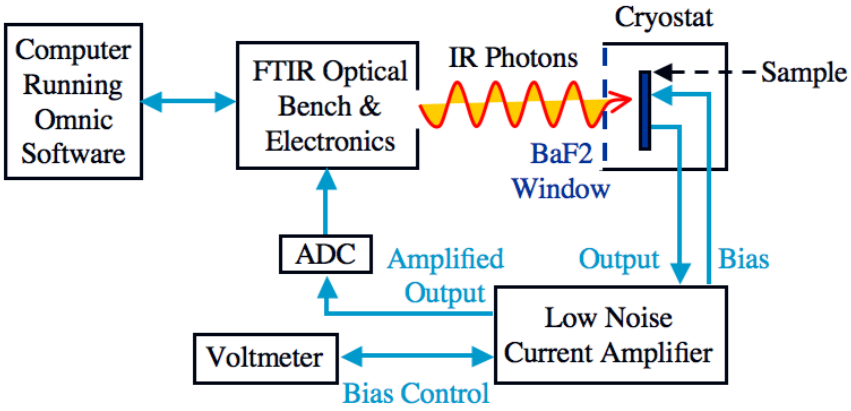

Figure 3.6: Spectral response measurement experimental set-up. A device from the sample replaces the normal detector in the FTIR system. The signal from the QDIP is amplified and sent through an analogue-to-digital converter into the FTIR electronics. A personal computer handles the data acquisition and calculates the Fourier transform.

normalisation of the spectral response by the peak wavelength of the spectrum, providing the normalised responsivity, $R'(\lambda)$. This data was obtained through measurements carried out previously using FTIR spectroscopy. The second measurement is of the photocurrent, I_{signal}, induced by normally incident IR radiation from a calibrated blackbody source.

The measurements for the QDIP photocurrent and noise signals for varying bias voltages were combined within a single experimental setup. For the dual measurement, the QDIP sample was mounted on a chip carrier inside a cryostat cooled with liquid nitrogen to a temperature of 77K, as above. The responsivity of each QDIP to normally incident IR radiation was calibrated using an 800°C (1073K) blackbody source. An optical chopper was used to modulate the incident radiation at a frequency of 140Hz. The modulated radiation provided a photocurrent signal that could be locked in to a specific frequency not associated with known electrical noise, such as the multiples of 50Hz corresponding to the power supply harmonics.

A Germanium crystal was attached to the front of the blackbody aperture to act as a high-pass optical filter. The Ge filter removed near-IR radiation with wavelengths less than 1.8μm emitted from the blackbody source. The output current from the device in the QDIP sample was then amplified through a SRS-570 low noise current pre-amplifier, which was also responsible for applying the bias voltage.

The photocurrent was initially measured using the setup shown in figure 3.7. This measurement was done by manually locking a SRS SR830 DSP lock-in amplifier to the signal corresponding to the chopper frequency and noting the measurement in a lab book. The output from the pre-amplifier was then disconnected from the lock-in and routed into a Hewlett Packard HP35665A dynamic signal analyser. The noise current was measured and also noted in the lab book. The pre-amplifier sensitivity and the bias applied to the

device were adjusted manually for each measurement, using a multimeter for the voltage readings.

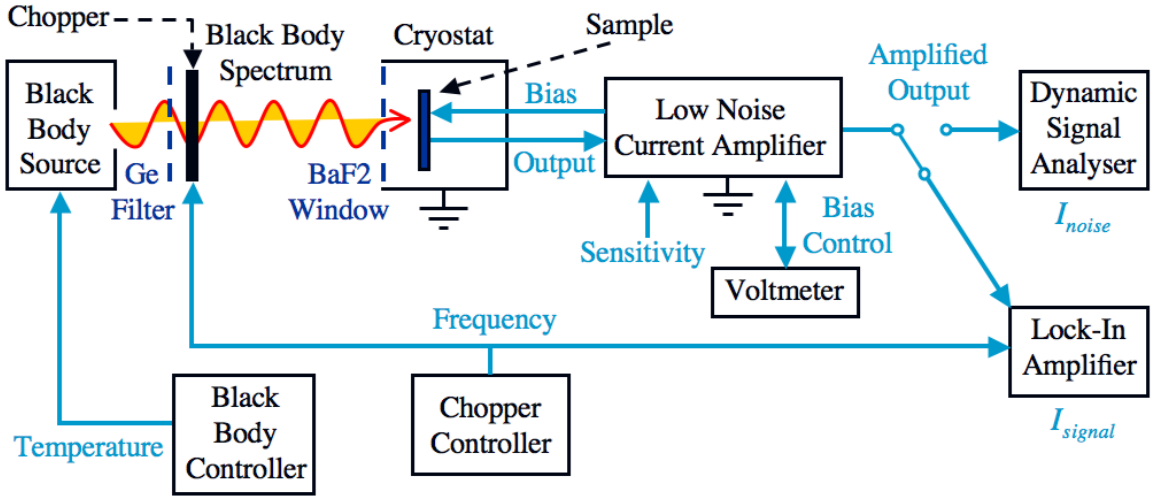

Figure 3.7: Initial noise and photocurrent measurement experimental set-up. The detector noise (I_{noise}) and response (I_{signal}) from a calibrated blackbody source are recorded by hand.

After becoming frustrated with the time necessary for these measurements and the subsequent data entry in Excel, a computer controlled version of the experimental setup was designed and implemented. The full experimental setup is shown in figure 3.8. The lock-in amplifier was replaced with a SRS SR 760 FFT spectrum analyser and an entire computer control and data acquisition program was written in the NI LabView graphical development environment. This new experimental setup simultaneously measured the photocurrent signal and the noise current signal, automatically performing the bias sweep and sensitivity adjustments. The time taken for these measurements was reduced from several hours down to less than half an hour, with additional time saved through the computer acquisition of the data. An overview of LabView and the automated noise measurement program is detailed in appendix A.

Calculation of the peak responsivity requires the data from the FTIR measurement and the photocurrent signal measurement. We start by looking at the full radiant power incident on the detector in the experimental setup, which can be expressed as:

$$Q(\lambda) = M_F \mathcal{T}_{Ge} \mathcal{T}_{BaF_2} \frac{\Omega}{\pi} \left(M(\lambda, T)_{BB} - M(\lambda, T)_{CH} \right) \tag{3.2}$$

$Q(\lambda)$ is determined by the chopper geometric modulation factor (M_F), solid angle of the light received (Ω), Ge filter & BaF_2 window transmittances ($\mathcal{T}$) and the spectral exitances ($M(\lambda, T)$) for the blackbody source and the chopper. The blackbody is calibrated for emission as a 1073K temperature source and the chopper has the spectrum for room

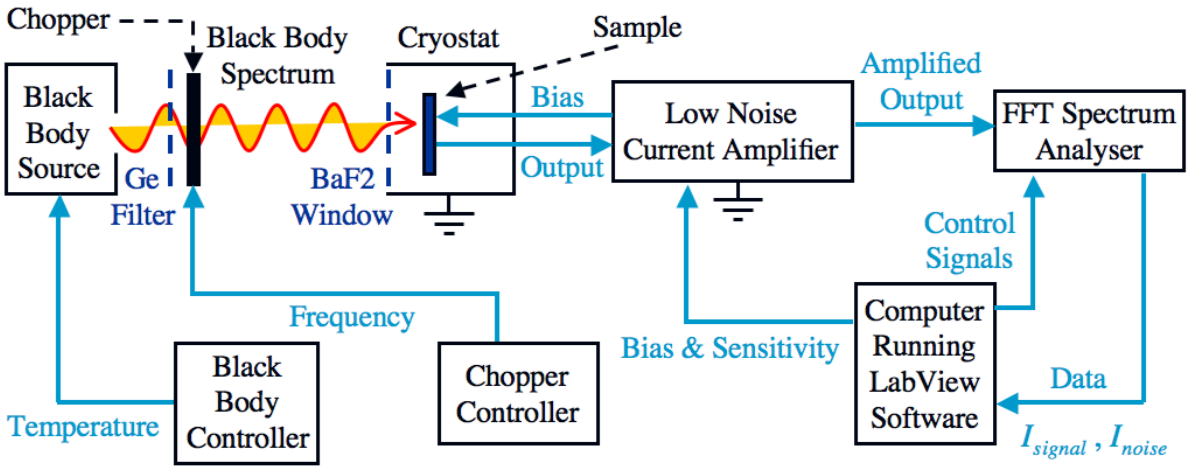

Figure 3.8: Computer-controlled noise and photocurrent measurement set-up. The detector noise (I_{noise}) and response (I_{signal}) from a calibrated blackbody source are recorded by computer.

temperature emission, 300K.

The spectral exitances, $M(\lambda,T)_{BB}$ & $M(\lambda,T)_{CH}$, are described by Planck's spectral excitance law, which states how radiant heat transfer depends upon temperature (T) and wavelength (λ):

$$M(\lambda,T) = \frac{2\pi c}{\lambda^4\left(e^{\frac{hc}{\lambda kT}}-1\right)} \tag{3.3}$$

where $c = 3\times10^8$m/s is the speed of light, $k = 5.67\times10^{-12}$Wcm^{-2}K^{-4} is the Boltzmann constant, and $h = 6.63\times10^{-34}$Js is Planck's constant.

The peak responsivity can now be determined from the photocurrent and normalised responsivity data, using the following equation derived from equations (3.1), (3.2) & (3.3):

$$R_{peak} = \frac{I_{signal}\lambda_{peak}}{hcM_F\mathcal{T}_{Ge}\mathcal{T}_{BaF_2}\frac{\Omega}{\pi}\int_0^\infty \frac{R'(\lambda)}{\lambda^4}\left(\frac{1}{\left(e^{\frac{hc}{1073\lambda k}}-1\right)}-\frac{1}{\left(e^{\frac{hc}{300\lambda k}}-1\right)}\right)d\lambda} \quad \text{(Amps/Watt)} \tag{3.4}$$

with λ_{peak} as the peak wavelength.

3.6.3 Specific Detectivity

The signal from a photodetector is always affected by shot noise and thermal noise. The specific detectivity, D^*, of a detector is a measure of the detectors signal-to-noise ratio, defined as:

$$D^* = \frac{R_{peak}}{I_{noise}}\sqrt{A\Delta f_{noise}} \tag{3.5}$$

where we have the peak responsivity, R_{peak}, the measured noise current, I_{noise}, detector area, A, and the measurement bandwidth, Δf_{noise}.

The detectivity is the most important figure of merit for characterising photodetectors. It immediately gives us a measure of the detectors quality, normalised by the detector area and measurement bandwidth.

The responsivity and noise current necessary for calculation of the detectivity for each sample were determined using the experiments in figures 3.7 & 3.8. A bias sweep was applied to each sample and the noise current was measured at each point in the sweep. The noise current was taken as the average of 50 measurements of the noise level centred at 625Hz over a bandwidth of 20Hz. The central frequency and bandwidth were simply chosen to avoid known environmental noise signals not corresponding to any intrinsic detector operation, such as the power supply harmonics (multiples of 50Hz).

3.6.4 Dark Current Density

The dark current density, J_{dark}, is defined as the current flowing through the detector when there is no incident radiation, divided by the metal contact area.

In order to measure the dark current, the chip carrier with a QDIP sample was mounted inside a fully-enclosed temperature-controllable cryostat. The chip-carrier was secured by contact-bonding the base of the chip-carrier with silver paste to the mount in the cryostat, followed by soldering the chip-carrier pins to the cryostat output pins. The cryostat was then inverted and immersed in liquid nitrogen, cooling the whole system down to 77K.

A computer controlled I-V measurement was then carried out (figure 3.9), with a bias sweep applied to the device, and the current measured with a Hewlett Packard 4140B pA meter/DC voltage source. The temperature of the chip carrier was raised in increments up to room temperature (290K) to allow a temperature dependent measurement. Control of this temperature sweep was provided by using a SemiTRAP DLS Controller 82E-3 with an accuracy of $\approx \pm 1$K for any given reading.

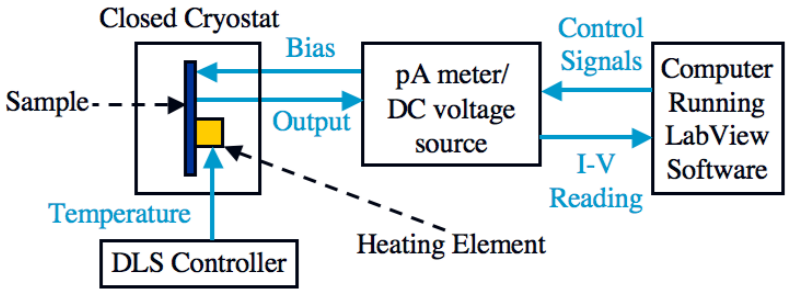

Figure 3.9: Dark current measurement experimental set-up. The I-V characteristic of the detector with no incident infrared radiation is measured and logged on computer. Between each measurement the temperature is raised using the DLS controller.

Chapter 4

Thermal Interdiffusion of Quantum Dot Infrared Photodetectors

4.1 Overview of this Chapter

In this chapter we present the results of a study of thermal interdiffusion of quantum dot infrared photodetectors. The nature of the study and the spectral response results are presented first. Then discussion of interdiffusion effects on the dark current density, responsivity, and detectivity gives us a picture of the overall performance of rapid thermal annealed QDIPs.

4.2 Rapid Thermal Annealing of QDIPs

As mentioned previously, little work has been done in studying the effects of interdiffusion on quantum dot devices' full performance. Thermal interdiffusion by post-growth annealing is an attractive method for the wavelength tuning of quantum well and dot devices. For this reason, a study of the effects of rapid thermal annealing on the device characteristics of quantum dot infrared photodetectors was carried out. Of particular interest at the commencement of the study were the temperatures necessary to initiate interdiffusion, and whether the subsequent wavelength shift in the device would be large enough to allow the fabrication of a two-colour detector.

As described in Chapter 3, a 10-layer quantum dot structure was grown and separated into a series of samples. These QD structures were each annealed at different temperatures and processed into QDIPs. The annealing temperatures were 600°C, 650°C, 700°C, 750°C, and 800°C, each for 30 seconds. Each annealed QDIP sample then underwent a detailed characterisation process to gain an understanding of the devices' performance after undergoing annealing, and determine the magnitude of the wavelength shift.

4.3 Annealed QDIP Spectral Responses

The results of the spectral response measurements at 77K are presented in figure 4.1. The normalised spectral responses of the annealed QDIPs , along with that of the as-grown sample are plotted in the one figure. The annealed QDIPs spectra have each been vertically shifted so that all the spectral responses can be compared simultaneously.

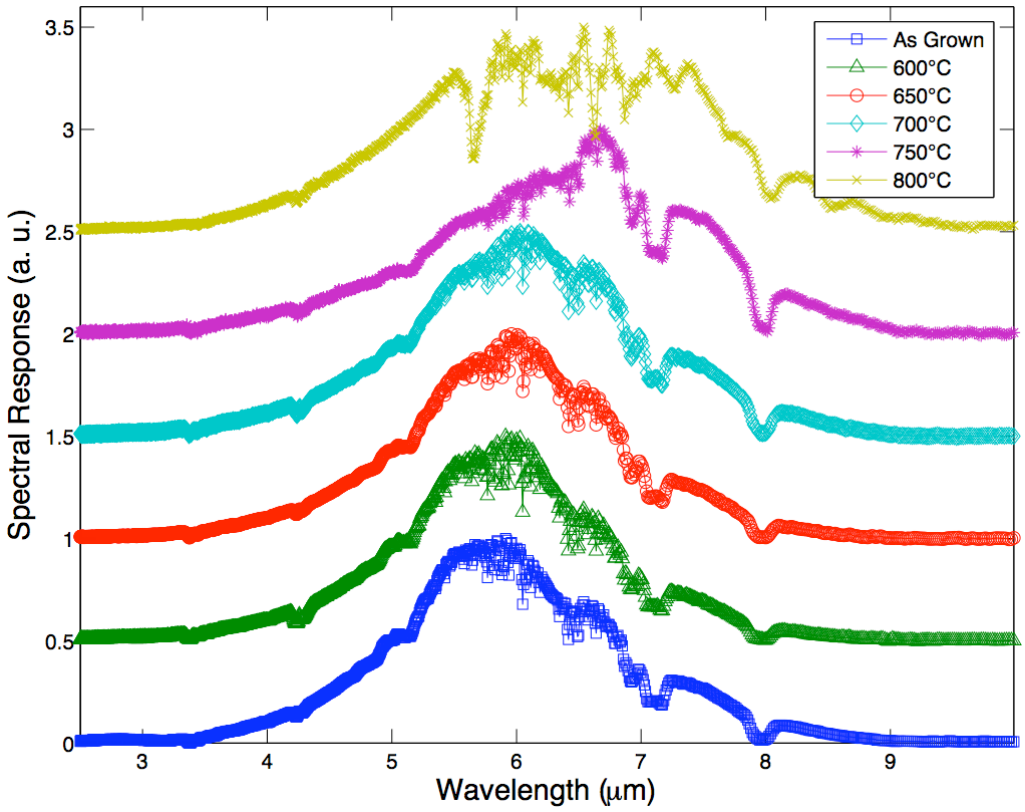

Figure 4.1: Normalised spectral responses from the annealed QDIPs at 77K compared with the as-grown QDIP.

It can be seen that redshifting of the peak wavelength only occurs for annealing temperatures above 650°C. The largest redshift occurs for an annealing temperature of 800°C, however with a large amount of spectral broadening. Thermal interdiffusion in the quantum dot structures has modified the shape of the confinement potential and reduced the intersubband transition energy for the high temperature annealed detectors. Another feature of the results is that the spectral responses lie almost entirely in the atmospheric absorption band between the two, so called, 'atmospheric windows' (3-5μm & 8-14μm bands). This positioning of the responses is unfortunate, but due to the inherent difficulty in the growth of self-assembled quantum dot structures it is hard to predict and control the peak operation wavelength of a detector.

The 800°C annealed sample showed the largest amount of interdiffusion, with sub-

stantial spectral broadening. The spectral broadening is due to the presence of two peaks in the spectrum, at 5.90μm & 7.08μm, respectively. The peak wavelength values were determined by fitting a double Lorentzian curve to the spectrum, as shown in figure 4.2, where the two Lorentzians and their sum are superimposed on the spectral response data. The extra peak in the spectrum at the shorter wavelength is a result of the large amount of interdiffusion. As a result, some of the Indium outdiffuses from the quantum dots, reducing the QD's Indium content. This change in the dot's composition has altered the distribution of the energy states within the quantum dots, leading to the appearance of the higher energy (shorter wavelength) absorption peak in the QDIP active region.

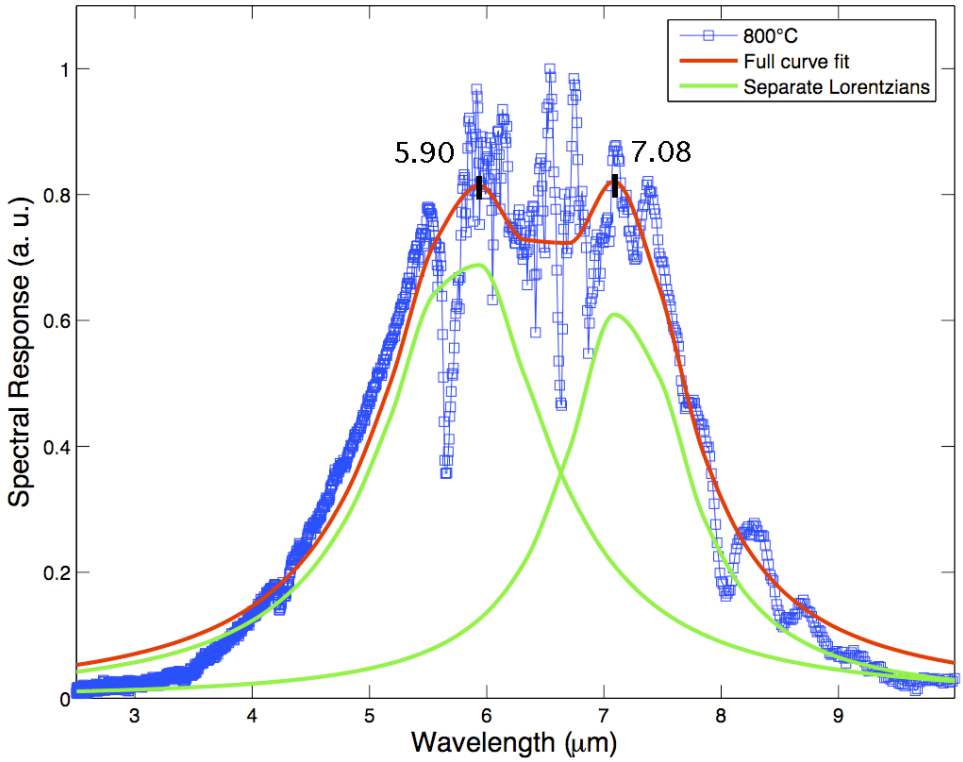

Figure 4.2: Lorentzian curves fitted to the 800°C annealed spectral response using the Microcal Origin software package. The red curve is composed of the sum of the two green Lorentzian curves. The peak wavelengths for the two peaks have been marked.

The peak wavelengths for all the annealed QDIPs are shown in table 4.1, from which it can be seen that the largest redshifts relative to the as-grown sample were 1.18μm for a 800°C anneal and 0.76μm for a 750°C anneal. The lower temperature annealed devices show a negligible amount of peak wavelength shift. The table also shows the peak operating bias drifting with the different annealing temperatures. The small amount of shifting in the 650°C sample is indicative of this annealing temperature being close to the temperature at which thermal interdiffusion begins to activate.

QDIP Sample	λ_{peak} (μm)	λ Shift (μm)	**Bias** (V)
As-Grown	5.90	-	0.4
600°C, 30s	5.90	0	0.45
650°C, 30s	5.95	0.05	0.45
700°C, 30s	6.02	0.12	0.4
750°C, 30s	6.66	0.76	0.35
800°C, 30s	7.08	1.18	0.35

Table 4.1: Peak operation wavelength and bias for the annealed and as-grown QDIPs. The wavelength shift relative to the as-grown sample is also included.

4.4 Dark Current Density of the Annealed Devices

The dark current is the current in the detector when there is no incident IR radiation. The dark current present in QDIPs has no satisfactory model as yet (Towe & Pan 2000), but appears to be due to the same sources as in quantum well devices.

There are three mechanisms, as shown in figure 4.3. Firstly, there is a classical thermionic component in which carriers are thermally excited to the continuum of states above the confining potential well. The second source is a thermally assisted tunnelling component, where carriers are thermally excited to higher energy states below the top of the well. From these states they can tunnel through the tip of the barrier into the continuum of states on the other side.

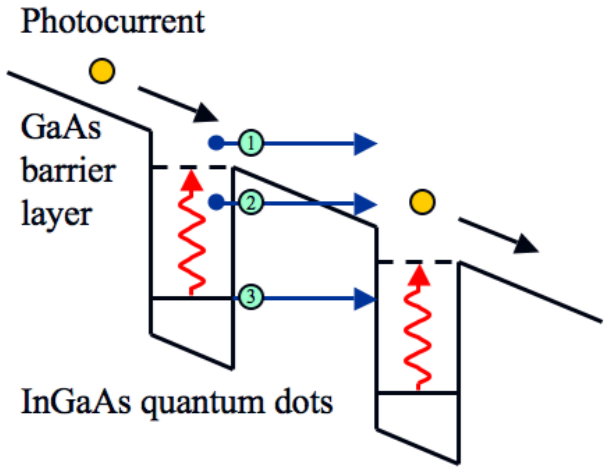

Figure 4.3: Schematic diagram of the dark current mechanisms in a QDIP under an external electric field. The three mechanisms are: (1) thermionic emission, (2) thermally assisted tunnelling, and (3) ground state sequential resonant tunnelling.

Finally, we have the temperature independent component of the dark current, that dominates at very low temperatures (<30K) as the other effects are reduced. This component comes from ground state carriers' sequentially resonant tunnelling between the 3-

dimensional wells of adjacent dots. Overall, this means that the temperature behaviour of the dark current in QDIPs is a nonlinear relation, when the mechanism is not thermionic.

The low temperature dark current I-V characteristics for the annealed samples compared with the as-grown sample are shown on a log scale in figure 4.4. This plot shows the dark current density as a function of the applied bias at a temperature of 77K. The effect of interdiffusion on the samples can be clearly seen as increases in the dark current with annealing temperature. It can be seen that the low temperature annealed samples (600°C & 650°C) and the 700°C sample have a similar dark current to the as-grown sample, while the 750°C & 800°C QDIPs have over an order of magnitude higher dark current from the strong interdiffusion effect.

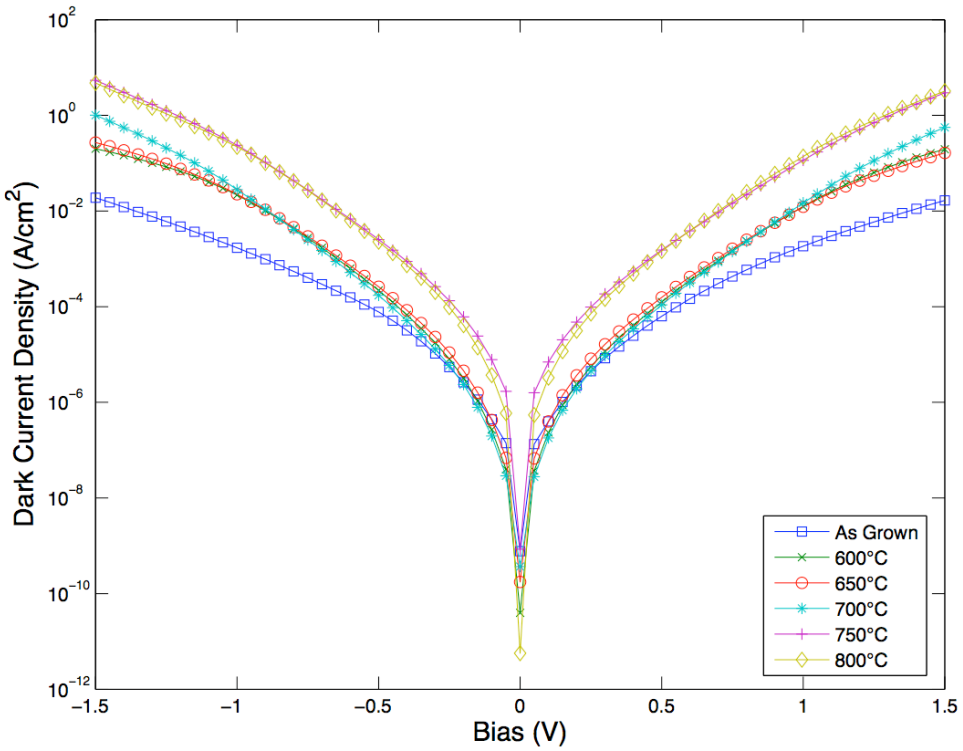

Figure 4.4: Dark current (IV) characteristic of annealed QDIPs vs bias at 77K compared with the as-grown QDIP.

It is well known that thermal annealing normally removes defects from a semiconductor material, but in the highly strained QD stacks such as QDIPs, strain relaxation may occur at high annealing temperatures. Strain relaxation results in the formation of extended defects such as dislocations, which will act to increase the dark current in the structure. The higher dark current levels in the high temperature annealed samples indicates that the interdiffusion may start to cause strain relaxation by the formation of extended defects. In addition, the elevated ground state in the high temperature annealed samples will also cause an increase in dark current.

Figure 4.5 shows the dark current density as a function of inverse temperature for a bias of 0.1V. This low bias is enough for QDIP operation, but not enough for the electric field to significantly alter the shape of the potential profile. The increased dark current of the 750°C & 800°C devices is clearly seen at all temperatures. The 700°C sample, in which interdiffusion is just becoming obvious, exhibits mixed behaviour. It has a similar dark current to the as-grown for the low temperatures (1000/T >7 K^{-1}), and a higher dark current at the higher temperatures. The lower dark current of the 600°C & 650°C QDIPs than the as-grown for a broad temperature range indicates that the low temperature annealing has reduced the defect density in the QDIP structure.

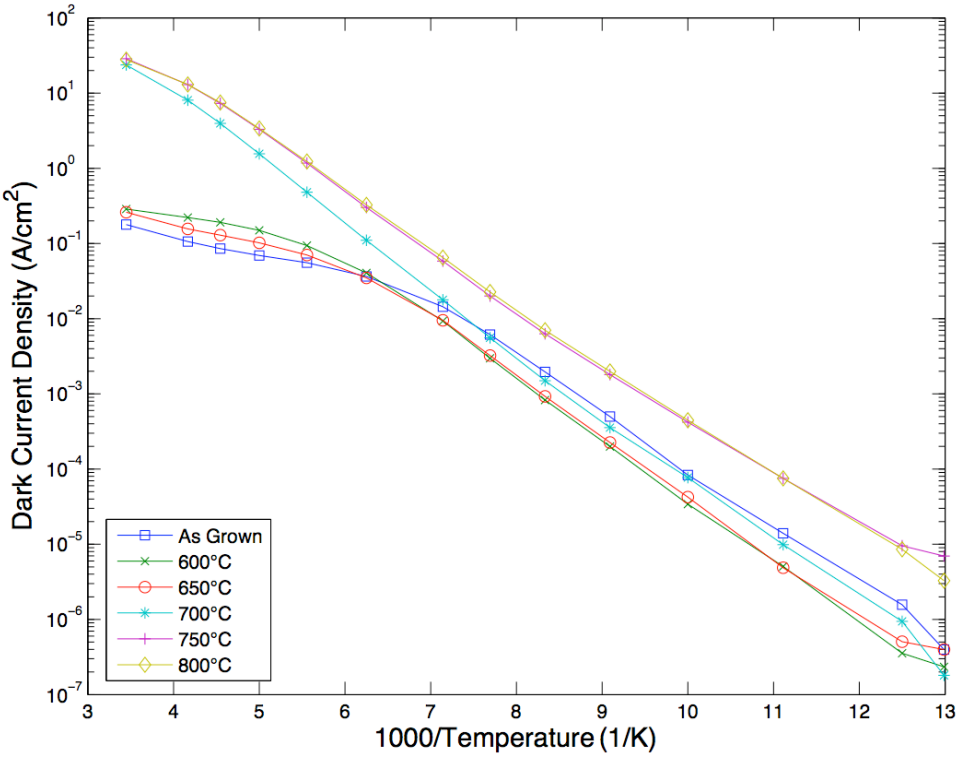

Figure 4.5: Dark current density of annealed QDIPs vs inverse temperature (1000/T) at a bias of 0.1V.

The Arrhenius ($J = J_0 e^{-E_a/KT}$) relation for dark current can be used to calculate the activation energy (E_a) of a QDIP proportional to the slope on the plot in figure 4.5. This relation is valid provided that the data exhibits linear behaviour, and our results are certainly not linear over the whole temperature range. If one looks only at the linear portion of the data it can be seen that the 750°C & 800°C annealed devices have a smaller slope than the as-grown, indicating a reduction in activation energy. This reduction is because the ground state in the intersubband transition has been raised higher up in the potential profile due to the interdiffusion. We can see this effect in the observed reduction of bias necessary for peak operating performance, relative to the as-grown sample, for

the 750°C & 800°C devices (see table 4.1). Close observation shows that the opposite effect can be seen for the 600°C & 650°C samples, with an increase in activation energy as confirmed by observation of their higher operating biases.

4.5 Peak Responsivities and Specific Detectivities

A comparison of the peak responsivity of the as-grown and annealed samples is displayed in figure 4.6, showing the bias dependence at 77K. There is very little difference in the responsivity of the annealed QDIPs and that of the as-grown device. The lower temperature anneals have slightly improved the responsivity by increasing it. Overall, the values for the responsivity are quite low, and this may be because the states in the QDs are not completely filled with carriers, since the dots are undoped. Additionally, the dots in our QDIP structure have a relatively large width-to-height ratio (see section 3.2 for the average height and width of 3.1nm and 18.9nm), leading to less confinement in the substrate plane. As a result, the detector is less sensitive to the polarisations of normally incident light (Fu et al. 2005). A slight asymmetry in the responsivity with bias can be observed in the curves, and is also to be seen in figure 4.7 for the detectivity. The asymmetry with bias is due to the asymmetric shape of the quantum dots in the active region of the detectors.

Figure 4.7 shows the low temperature signal-to-noise ratio (detectivity) vs bias. While the responsivity was fairly unchanged for the annealed devices, the detectivity shows more variation. For the temperatures below the interdiffusion activation temperature (600°C & 650°C), the detectivity shows a slight increase. The 700°C, 750°C, & 800°C annealed devices each show a successive reduction in the detectivity over the whole bias range.

The peak detectivities and their operating bias, along with the corresponding responsivities for the devices are listed in table 4.2.

QDIP Sample	**Responsivity** (mA/W)	**Detectivity** ($cmHz^{1/2}/W$)	**Bias** (V)
As-Grown	4.788	1.302×10^{9}	0.4
600°C, 30s	6.085	1.485×10^{9}	0.45
650°C, 30s	6.570	1.676×10^{9}	0.45
700°C, 30s	3.596	8.437×10^{8}	0.4
750°C, 30s	2.88	5.929×10^{8}	0.35
800°C, 30s	1.793	2.955×10^{8}	0.35

Table 4.2: Peak operating values for the specific detectivity and the corresponding responsivity and bias for the annealed and as-grown QDIPs.

It is worth noting that for the higher annealing temperatures, the detectivity was reduced while the responsivity was not significantly changed. This behaviour is due to

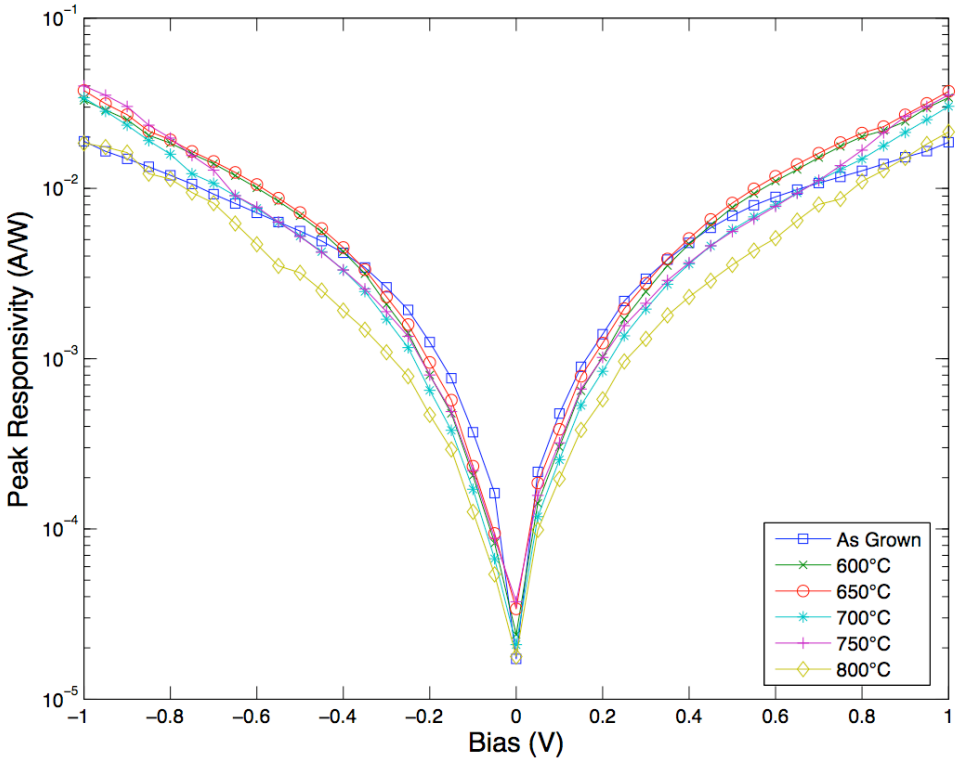

Figure 4.6: Peak responsivity of annealed QDIPs vs bias at 77K compared with the as-grown QDIP.

the different effects of thermal interdiffusion. As mentioned earlier, high temperature annealing will cause a reduction in the activation energy of the samples, as well as the formation of extended defects due to strain relaxation. The rise in activation energy results in the presence of more photocurrent and more dark current. Extended defect formation causes a reduction in the photocurrent by trapping carriers, and an increase in dark current.

Therefore, as a result of balancing in these two effects, the responsivity of the annealed detectors did not change significantly. However, as dark current increased with rising annealing temperature in figure 4.5, the detectivity of the devices was reduced.

However, it is worth mentioning that the degradation in performance indicated by lower responsivity and detectivity is quite small and much less significant compared with the responsivity values reported in (Hwang et al. 2005*b*). We ascribe this performance to the better quality quantum dot growth achieved in this work. Even the most heavily interdiffused sample (800°C annealed) still shows only a small reduction in detectivity and in responsivity.

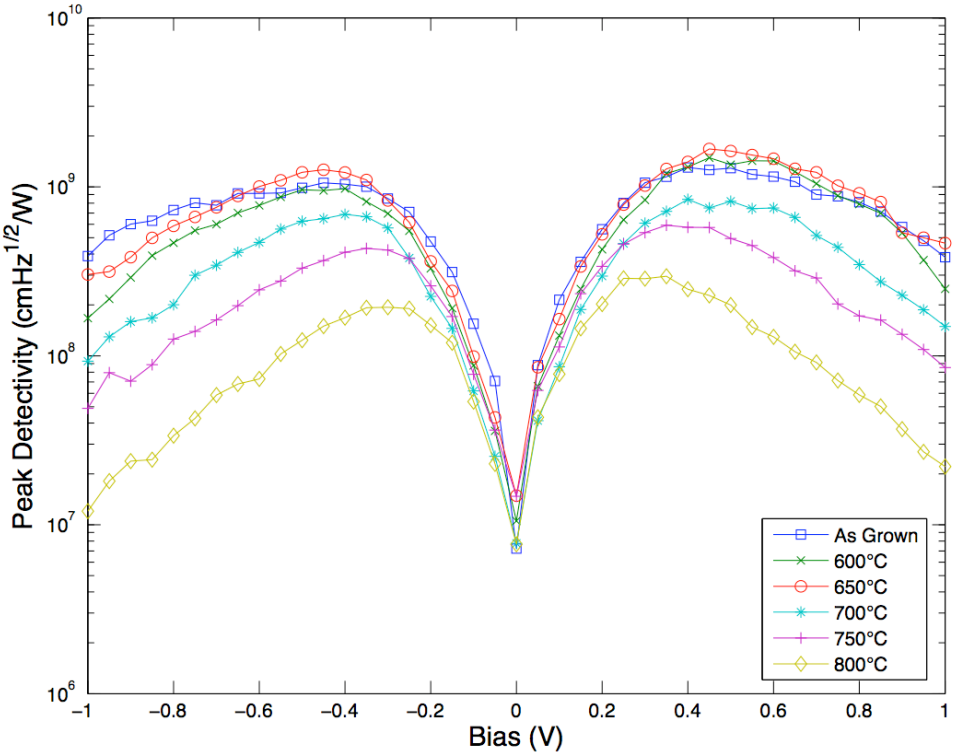

Figure 4.7: Specific detectivity of annealed QDIPs vs bias at 77K compared with the as-grown QDIP.

4.6 Conclusion

A significant redshift in the operating wavelength of the QDIPs was seen for high temperature anneals. This shift corresponded with an increase in the detector dark current and a small reduction in responsivity & detectivity, compared to the as-grown sample. Taken as a whole, the degradation in device performance from thermal annealing was not significant. The performance can be further improved by optimisation of the growth quality of the stacked quantum dots in the QDIP structure. An annealing temperature of 800°C gave the largest wavelength redshift, with the disadvantage of large spectral broadening due to multiple transitions allowed in the active region. Annealing at 750°C provided a large shift in wavelength with minimal spectral broadening, and therefore was chosen as the annealing temperature for making the two-colour QDIP.

Chapter 5

Two-Colour Quantum Dot Infrared Photodetector

5.1 Overview of this Chapter

In this chapter the results of a study into the creation of a two-colour quantum dot infrared photodetector are presented. The details of the detector design are discussed first, after which the spectral response results are examined. We follow this appraisal by analysing the I-V characteristic, responsivity and detectivity of the two-colour detector.

5.2 Design of the Two-Colour QDIP

As discussed previously, multicolour IR detectors are desirable for the future high performance IR systems. In order to make a multicolour quantum dot infrared photodetector using thermal interdiffusion for wavelength tuning, the process must only redshift the wavelengths of selected pixels. The fabrication process must be able to suppress interdiffusion in the other pixels, keeping the wavelength unchanged during the high temperature annealing. It has been shown that the use of a dual layer TiO_2/SiO_2 dielectric film on the structure acts to effectively suppress interdiffusion within InGaAs/GaAs structures (Lever et al. 2004*a*, Fu et al. 2003).

Building on the understanding of the thermal interdiffusion of the 10-layer QD structure and the operating wavelength redshift, a two-colour quantum dot infrared photodetector was constructed. The design of the two-colour QDIP is presented in figure 5.1. It consisted of a wafer using the same 10-layer QDIP structure as in the thermal annealing study, with a bi-layer TiO_2/SiO_2 capping deposited on one half of the wafer to selectively suppress interdiffusion. The first layer was a very thin layer of SiO_2 deposited using PECVD, amounting to approximately 10$\sim$15nm thickness. Over the top of this, a 180nm layer of TiO_2 was deposited using electron beam evaporation, as described in chapter 3.

The purpose of having a thin SiO_2 layer underneath the TiO_2 was to make the removal of the titanium dioxide easy, through a simple chemical etching using hydrofluoric acid

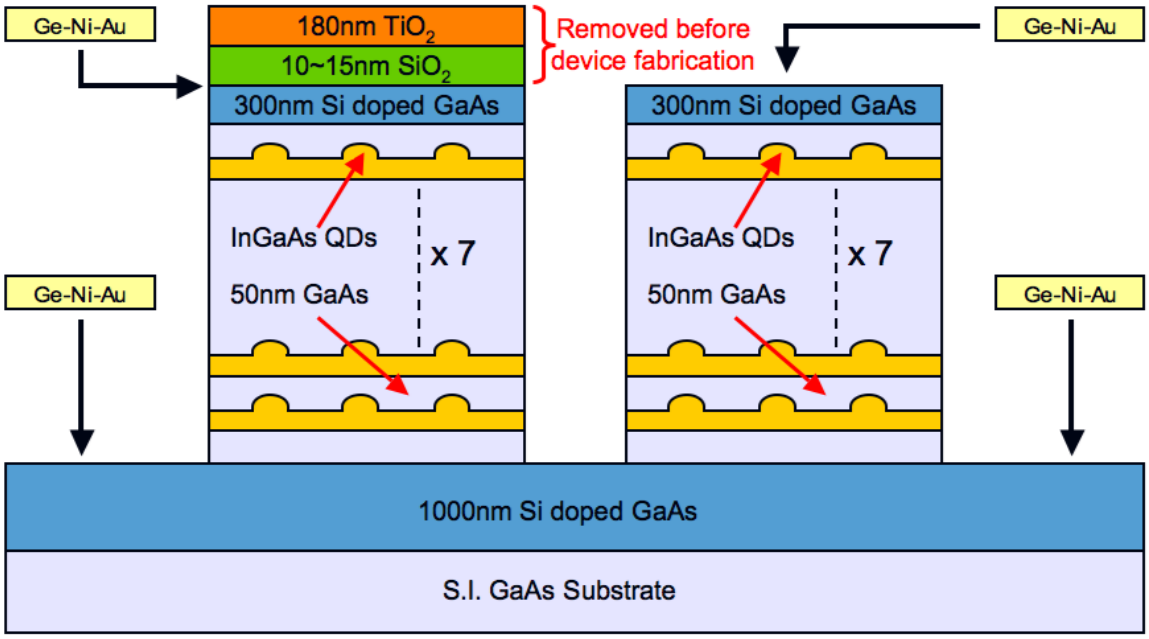

Figure 5.1: Cross-sectional schematic of the two-colour QDIP. One of the pixels has had a bi-layer film deposited on it, before the whole structure was annealed. The film was then removed and the metallisation processing performed, with the metal contacts in the locations indicated. The bi-layer capped pixel is also referred to as the TiO_2/SiO_2 capped device and the uncapped pixel also referred to as the 750°C device.

(HF). The layer of SiO_2 was too thin to affect the strong tensile stress applied by the TiO_2 due to its larger thermal expansion coefficient, which prohibits thermal interdiffusion in the structure.

The whole structure was then annealed in the EME RTA furnace at a temperature of 750°C for 30s. From the previous study we found that, compared with the as-grown sample, the 750°C annealed sample had a slightly smaller redshift than did the 800°C annealed device. However, it did not suffer from the large spectral broadening and performance degradation as the 800°C sample. This lack of broadening made 750°C the preferable annealing temperature for providing enough redshift to achieve two distinctly different operating wavelengths in the two-colour detector.

After the annealing, the TiO_2/SiO_2 layer was removed with 20% HF acid in water, and the whole sample was fabricated into QDIP devices. The separate TiO_2/SiO_2 capped and un-capped detectors underwent the detailed characterisation independently. For the purposes of discussion, the different QDIPs are referred to as the TiO_2/SiO_2, and 750°C annealed devices respectively for the comparison to the un-annealed, 'as-grown', sample.

5.3 Two-Colour Spectral Response

Looking at the spectral response results in figure 5.2, we can see the spectra for the two colour photodetector, along with the spectrum for the as-grown device. The successful suppression of the interdiffusion in the TiO_2/SiO_2 dielectric capped device can be seen clearly in the plot. The wavelength shift is almost non-existent, with a difference in peak values of $\approx 1\mu$m and no spectral broadening when compared with the un-annealed, as-grown sample. In comparison, the uncapped device exhibits a wavelength redshift of the spectral response peak position as a result of thermal interdiffusion. The separation in the two peaks of the two-colour detectors spectral responses is 0.75μm.

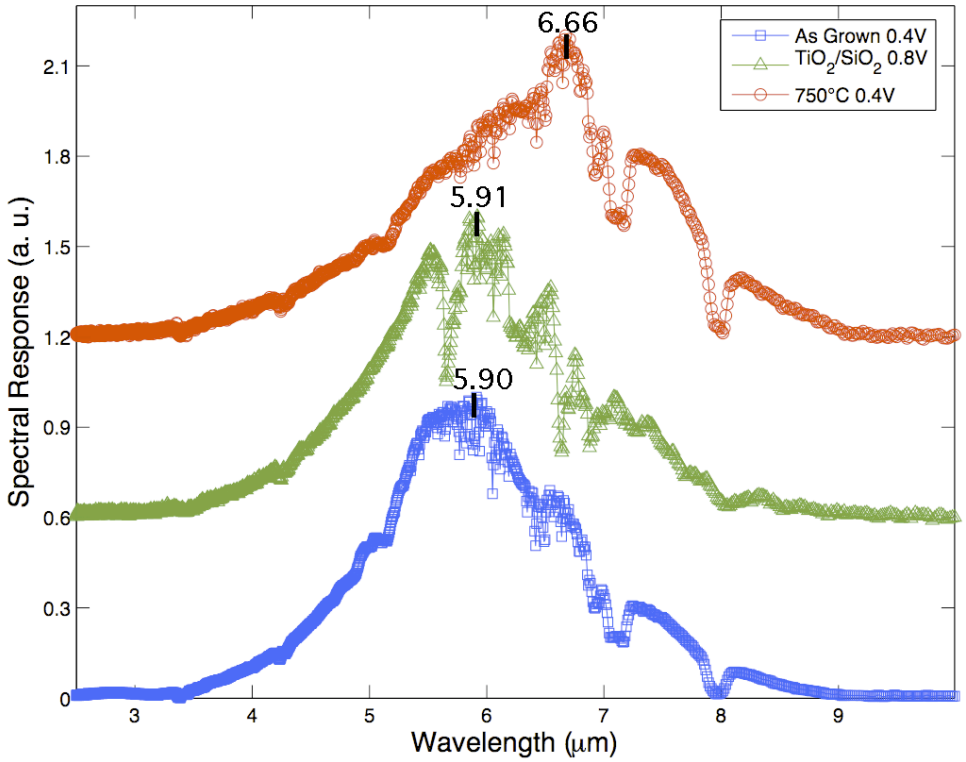

Figure 5.2: Spectral responses from the two-colour QDIP compared with the as-grown device, measured at 77K. The peak wavelengths of each spectrum are also labelled on each plot.

5.4 Performance of the Two-Colour QDIP

The dark current characteristic, peak responsivity, and the detectivity were all measured for the two-colour detector at low temperature. These results can be seen in figures 5.3, 5.4 and 5.5, where the characteristics for each device in the detector have been plotted as a function of bias.

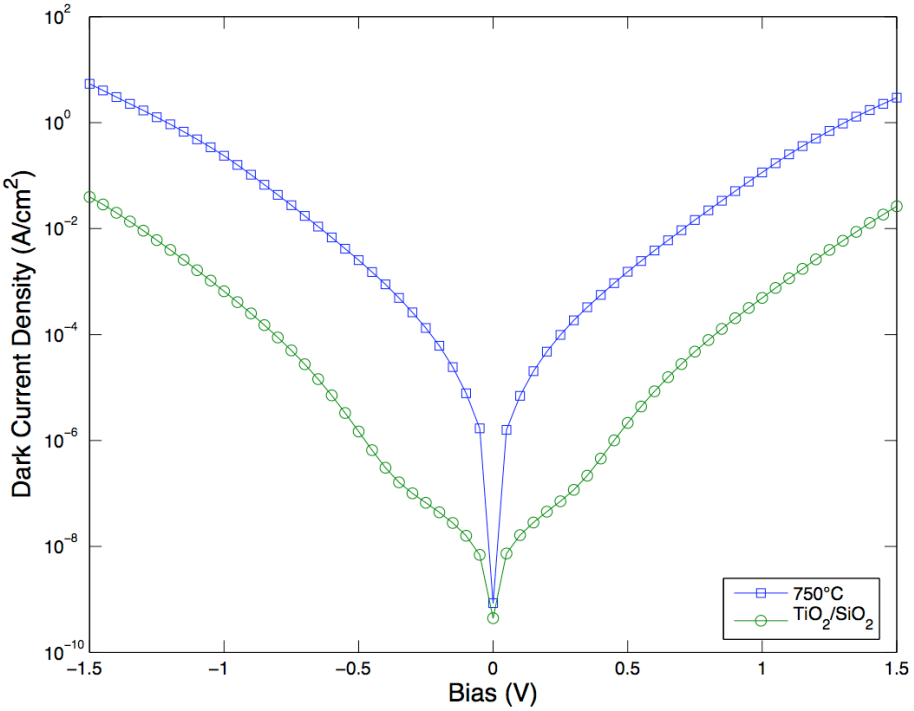

Figure 5.3: Dark current (IV) characteristics of the two-colour detector devices vs bias at 77K.

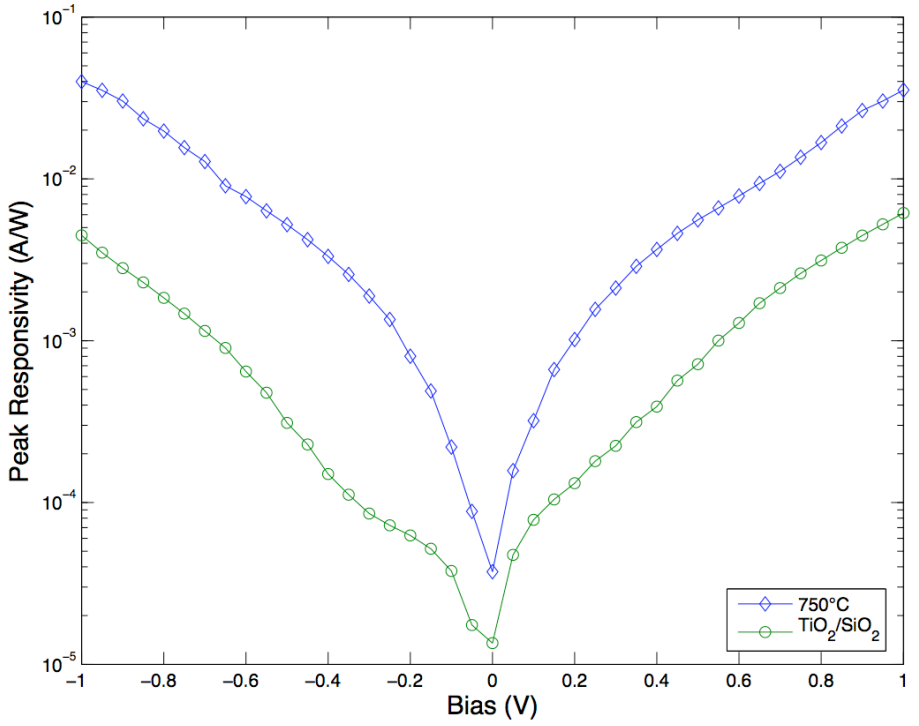

Figure 5.4: Peak responsivity of the devices in the two-colour detector vs bias at 77K.

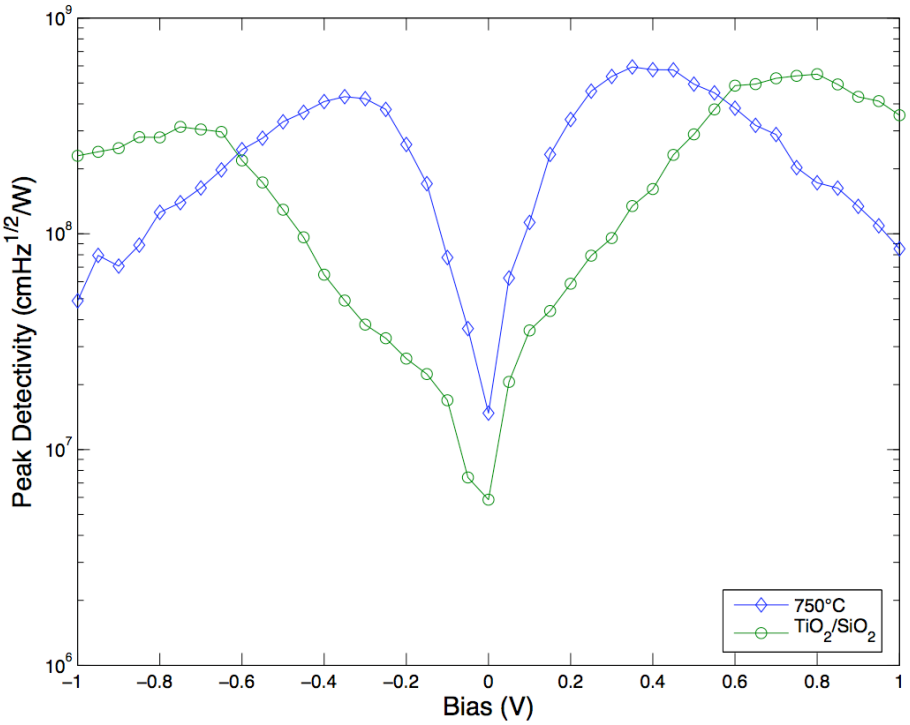

Figure 5.5: Specific detectivity of the devices in the two-colour detector vs bias at 77K.

A summary of the peak performance parameters for the two-colour QDIP is provided in table 5.1, along with the information for the as-grown device for comparison. A look at the performance parameters in the table show that there is very little difference in the two-colour devices' relative performance, as indicated by their similar responsivities and detectivities.

QDIP Device	**Dark Current Density** (A/cm^2)	**Responsivity** (mA/W)	**Detectivity** ($cmHz^{1/2}/W$)	**Bias** (V)
As-Grown	2.478×10^{-5}	4.788	1.302×10^{9}	0.4
750°C	3.282×10^{-4}	2.882	5.929×10^{8}	0.35
TiO_2/SiO_2	7.88×10^{-5}	3.129	5.495×10^{8}	0.8

Table 5.1: The peak detectivity and corresponding dark current density, peak responsivity, and bias for the devices in the two-colour detector compared with the as-grown QDIP.

It also is noted that in all the measurements, the TiO_2/SiO_2 bi-layer device required a higher bias to exhibit performance similar to the un-capped device. This bias necessary (0.8V) to reach peak performance is double that of the other QDIPs made during this study ($\approx$0.4V).

We ascribe this behaviour to an increase in the series resistance of the bi-layer device's top contact. This resistance increase is believed to be due to a metallurgical reaction that

took place at the interface between the GaAs and the TiO_2/SiO_2 bi-layer.

The resistance increase has also skewed the direct comparison in the dark current and responsivity plots, since twice the bias must be applied to the bi-layer device to get operating conditions similar to that of the un-capped device. Hence, there is the appearance of differing performance in all the plots.

The difference in the two devices operating bias is undesirable for real applications, since it requires the two-colour detector to operate with a different bias for each pixel. A further study on two-colour detection carried out by the EME group has recently demonstrated that the use of a single capping layer of TiO_2, with a dry etching process to fabricate a similar two-colour detector. This detector produced after my project demonstrates none of the series resistance problems and operates under the same bias conditions as the un-capped device.

Comparing the TiO_2/SiO_2 capped device to the as-grown sample, using table 5.1 shows that there is a small degradation in the capped device's performance. Interdiffusion has been suppressed, however, as noted in the thermal interdiffusion study, high temperature annealing of the highly strained QD structures can cause the formation of extended defects. These extended defects have resulted in a small reduction in responsivity and detectivity, and an increase in the dark current of the bi-layer device, relative to the un-annealed sample. The dark current in the bi-layer device is still lower than that of the 750°C annealed device, which has had its ground state energy raised due to the interdiffusion causing an increase in dark current as discussed in the previous chapter.

It must be stressed that the overall performance of the two-colour detector is well maintained. The two devices in the detector display matching performance that is highly desirable for the purposes of large scale read-out integration, where uniform performance of the devices across the wafer is essential.

5.5 Conclusion

A two-colour quantum dot infrared photodetector was successfully demonstrated by selectively suppressing thermal interdiffusion using a TiO_2/SiO_2 bi-layer capping. The high temperature anneal initiated interdiffusion in the un-capped device, resulting in two different peak operating wavelengths for the different devices in the detector. Apart from a difference in operating bias, both devices demonstrated similar behaviour with respect to dark current, responsivity and detectivity. This consistency shows that this type of two-colour QDIP is suitable for readout integration in a focal plane array (FPA) system.

With appropriate mask design and fabrication processes, this method can easily be extended to make a focal plane array. The use of selective deposition of dielectric layers followed by a high temperature anneal could create an array with alternating pixels on

the same substrate having one of two different peak response wavelengths. The post growth process described here should have use in different imaging applications, with the advantages of simplicity and flexibility.

Chapter 6

Conclusion

6.1 Summary and Conclusions

In this thesis we have undertaken a comprehensive investigation of the effects of interdiffusion in quantum dot infrared photodetectors in order to achieve the main project goal of fabricating and characterising a two-colour infrared detector.

A series of ten-layer InGaAs/GaAs quantum dot infrared photodetectors grown by MOCVD were subjected to different amounts of thermal interdiffusion using rapid thermal annealing. They were fabricated into devices using standard semiconductor processing techniques and then underwent detailed characterisation involving the measurement of their spectral response, dark current, responsivity, and detectivity. An automated system for the measurement of the responsivity and detectivity was designed and implemented.

The annealed devices characterisation revealed that the two highest annealing temperatures induced a significant redshift in the operating wavelength of the QDIPs due to large interdiffusion in the structures. With increasing annealing temperature, the devices showed a slight reduction in performance due to the competition of effects in raising of the QDIP's ground state and the formation of extended defects. It was concluded that post-growth annealing is a viable process for wavelength tuning of QDIPs.

A two-colour quantum dot infrared photodetector was then successfully demonstrated. The detector was fabricated using selective deposition of a bi-layer TiO_2/SiO_2 film onto the QDIP structure to suppress the interdiffusion during rapid thermal annealing. Afterwards, the film was removed and the sample processed into QDIPs. Measurement of the two-colour photodetector characteristics showed that the two components of the detector exhibited similar operating performance, with a large difference of 0.75μm in peak operating wavelengths.

The work in this thesis has implications for the fabrication of two-colour QDIPs into focal plane arrays. The consistency in performance of the devices in the two-colour detector along with the simplicity and flexibility of the post-growth wavelength tuning makes FPA fabrication suitable. The design of a masking and fabrication process to selectively redshift alternating pixels on a substrate is a promising method for two-color FPA fabri-

cation, with use in applications such as thermal imaging and chemical analysis.

6.2 Future Work

Future work that needs to be done to improve the performance of the two-colour QDIP demonstrated in this study. The QDIP structure used as the basis for the detector may be improved with the use of strain-compensation layers between the dot layers to reduce the accumulated strain in the structure. This design may allow higher levels of interdiffusion by reducing the formation of extended defects during rapid thermal annealing. Another method for improving the structure is the introduction of n-type doping into the quantum dots. The effect of doping is an increase in the carriers occupying the states within the dots, with the effect of possibly increasing the photocurrent and hence the responsivity.

Research into the effects of differing numbers of quantum dot layers in the active region of the QDIP structure is also important. Increasing the number of QD layers in the stacked structure may improve performance by increasing the overall gain. The use of too many layers, however, may cause a large amount of strain accumulation that could have adverse effects on the device during thermal annealing.

The design of detectors with more than two colours can be investigated. Different of amounts interdiffusion suppression can be achieved by varying the relative thicknesses of the layers in the bi-layer TiO_2/SiO_2 film from the two-colour detector in this work. Therefore, variation of the thickness' would allow the control of the degree of wavelength shifting, enabling the fabrication of three or more colour detectors.

At the time of writing, the EME quantum dot optoelectronics group demonstrated a two-colour detector using purely TiO_2 capping. This detector exhibited the same behaviour as the two-colour detector in this study, with an improvement in the consistency of the different devices operating bias. Additionally, a study into the impurity free vacancy disordering of QDIPs using only SiO_2 capping carried out by the author of this thesis, is currently undergoing analysis of results.

Bibliography

Bimberg, D. & Ribbat, C. (2003), 'Quantum dots: lasers and amplifiers', *Microelec. J.* **34**, 323–328.

Chakrabarti, S., Stiff-Roberts, A. D., Bhattacharya, P., Gunapala, S., Bandara, S., Rafol, S. B. & Kennerly, S. W. (2004), 'High-temperature operation of InAs/GaAs quantum-dot infrared photodetectors with large responsivity and detectivity', *IEEE Photonic. Tech. Lett.* **16**(5), 1361–1364.

Chen, Z. H., Baklenov, O., Kim., E. T., Mukhametzhanov, I., Tie, J., Madhukar, A., Ye, Z. & Campbell, J. C. (2001), 'Normal incidence InAs/AlGaAs quantum dot infrared photodetectors with undoped active region', *J. Appl. Phys.* **89**, 4558–4563.

Eisberg, R. & Resnick, R. (1974), *Quantum Physics of Atoms, Molecules, Solids Nuclei, and Particles*, Wiley, New York.

Esaki, L. & Sakaki, H. (1977), 'New photoconductor', *IBM. Tech Disc Bull.* **20**, 2456–2457.

Fu, L. (2001), *Quantum Well Intermixing in (In)GaAs/(Al)GaAs Materials and Devices*, Australian National University. PhD Thesis.

Fu, L., Lever, P., Tan, H. H. & Jagadish, C. (2003), 'Suppression of interdiffusion in InGaAs/GaAs quantum dots using dielectric layer of titanium dioxide', *Appl. Phys. Lett.* **82**(16), 2613–2615.

Fu, L., Tan, H. H., McKerracher, I., Wong-Leung, J., Jagadish, C. & Vukmirović, N. (2005), Effects of rapid thermal annealing on device characteristics of InGaAs/GaAs quantum dot infrared photodetectors. Submitted to J. Appl. Phys.

Goldstein, L., Glas, F., Martin, J. Y., Charasse, M. N. & Roux, G. L. (1985), 'Growth by molecular beam epitaxy and characterisation of InAs/GaAs strained-layer superlattices', *Appl. Phys. Lett.* **47**(10), 1099–1101.

Gunapala, S. D., Bandara, S. V., Singh, A., Liu, J. K., Rafol, B., Luong, E. M., Mumolo, J. M., Tran, N. Q., Ting, D. Z. Y., d. Vincent, J., Shott, C. A., Long, J. & LeVan, P. D. (2000), '640×486 long-wavelength two-color GaAs/AlGaAs quantum

well infrared photodetector (qwip) focal plane array camera', *IEEE. Trans. Electron. Devices* **47**(5), 963–971.

Hwang, S. H., Shin, J. C., Song, J. D., Choi, W. J., Lee, J. I. & Han, H. (2005*b*), 'Detection wavelength tuning of InGaAs/GaAs quantum dot infrared photodetector with thermal treatment.', *Microelec. J.* **36**(3), 203–205.

Hwang, S. H., Shin, J. C., Song, J. D., Choi, W. J., Lee, J. I., Han, H. & Lee, S. W. (2005*a*), 'Characteristics of thermally treated quantum-dot infrared photodetector', *Jap. J. Appl. Phys.* **44**(7B), 5696–5699.

Jiang, J., Tsao, S., O'Sullivan, T., Zhang, W., Lim, H., Sills, T., Mi, K., Razeghi, M., Brown, G. J. & Tidrow, M. Z. (2004), 'High detectivity InGaAs/InGaP quantum-dot infrared photodetectors grown by low pressure metalorganic chemical vapour deposition', *Appl. Phys. Lett.* **84**(12), 2166–2168.

Kim, S. & Harris, J. (2004), 'Multicolor InGaAs quantum dot infrared photodetectors', *IEEE Photonic. Tech. Lett.* **16**(11), 2538–2540.

Krishna, S., Forman, D., Annamalai, S., Dowd, P., Varangis, P., Tumolillo, Jr, T., Gray, A., Zilko, J. & Sun, K. (2005), 'Demonstration of a 320×256 two-color focal plane array using InAs/InGaAs quantum dots in well detectors', *Appl. Phys. Lett.* **86**, 193501–193503.

Krishna, S., Raghavan, S., von Winckel, G., Rotella, P., Stintz, A., Morath, C. P., Le, D. & Kennerly, S. W. (2003), 'Two-color InAs/InGaAs dots-in-a-well detector with background-limited performance at 91K', *Appl. Phys. Lett.* **82**, 2574–2576.

Krishna, S., Raghavan, S., von Winckel, G., Stintz, A., Ariyawansa, G., Matsik, S. G. & Perera, A. G. U. (2003), 'Three-color $\lambda_{p1} \approx 3.8\mu m$, $\lambda_{p2} \approx 8.5\mu m$, and $\lambda_{p3} \approx 23.2\mu m$ InAs/InGaAs quantum-dots-in-a-well detector', *Appl. Phys. Lett.* **83**(14), 2745–2747.

Krishna, S., Stiff-Roberts, A. D., Phillips, J. D., Bhattacharya, P. & Kennerly, S. W. (2002), 'Hot dot detectors: Infrared quantum dot intersubband photodetectors are a promising technology for multiwavelength ir detection', *IEEE Circuits & Devices* **18**(1), 14–21.

Leon, R. & Fafard, S. (1998), 'Structural and radiative evolution in quantum dots near the $In_xGa_{1-x}As/GaAs$ stranski-krastanow transformation', *Phys. Rev. B* **58**(4), 1726–1729.

Leon, R., Kim, Y., Jagadish, C., Gal, M., Zou, J. & Cockayne, D. J. H. (1996), 'Effects of interdiffusion on the luminescence of InGaAs/GaAs quantum dots', *Appl. Phys. Lett.* **69**(13), 1888–1890.

Lever, P. (2004), *Interdiffusion and MOVPE Growth of Self-Assembled InGaAs QD Structures and Devices*, Australiam National University. PhD Thesis.

Lever, P., Fu, L., Tan, H. H., Jagadish, C., Reece, P. & Gal, M. (2003), 'Comparison of interdiffusion between single and stacked-layer InGaAs/GaAs quantum dots'. Proceedings of the Third IEEE Conference on Nanotechnology, San Francisco, USA.

Lever, P., Tan, H. H. & Jagadish, C. (2004*a*), 'Impurity free vacancy disordering of InGaAs quantum dots', *J. Appl. Phys.* **96**(12), 7544–7548.

Lever, P., Tan, H. H. & Jagadish, C. (2004*b*), 'InGaAs quantum dots grown with GaP strain compensation layers', *J. Appl. Phys.* **95**(10), 5710–5714.

Liu, H. C., Gao, M., Mcaffrey, J., Wasilewski, Z. R. & Fafard, S. (2001), 'Quantum dot infrared photodetectors', *Appl. Phys. Lett.* **78**(1), 79–81.

Pan, D., Towe, E. & Kennerly, S. (1998), 'normal-incidence intersubband (In,Ga)As?GaAs quantum dot infrared photodetectors', *App. Phys. Lett.* **73**(14), 1937–1939.

Phillips, J., Bhattacharya, P., kennerly, S. W., Beekman, D. W. & Dutta, M. (1999), 'Self-assembled InAs-GaAs quantum-dot intersubband detectors', *IEEE J. Quant. Electron.* **35**(6), 936–942.

Raghavan, S., Forman, D., Hill, P., Weisse-Bernstein, N. R., von Winckel, G., Rotella, P., Krishna, S., Kennerly, S. W. & Little, J. W. (2004), 'Normal-incidence InAs/$In_{0.15}Ga_{0.85}As$ quantum dots-in-a-well detector operating in the long-wave infrared atmospheric window ($812\mu m$)', *J. Appl. Phys.* **96**(2), 1036–1039.

Ryzhii, V. (1996), 'The theory of quantum-dot infrared phototransistors', *Semicond. Sci. Technol.* **11**, 759–765.

Sakoglu, U., Tyo, J. S., Hayat, M. M., Raghavan, S. & Krishna, S. (2004), 'Spectrally adaptive infrared photodetectors with bias-tunable quantum dots', *J. Opt. Soc. Am. B* **21**(1), 7–17.

Saleh, B. E. A. & Teich, M. C. (1991), *Fundamentals of Photonics*, John Wiley and Sons, Inc, New York.

Sarusi, G., Levine, B. F., Pearton, S. J., Bandara, K. M. S. & Leibenguth, R. E. (1994), 'Improved performance of quantum well infrared photodetectors using random scattering optical coupling', *Appl. Phys. Lett.* **64**(8), 960–962.

Stewart, K., Buda, M., Wong-Leung, J., Fu, L., Jagadish, C., Stiff-Roberts, A. & Bhattacharya, P. (2003), 'Influence of rapid thermal annealing on a 30 stack InAs/GaAs quantum dot infrared photodetector', *J. Appl. Phys.* **94**(8), 5283–5289.

Stiff, A. D., Krishna, S., Bhattacharya, P. & Kennerly, S. W. (2001), 'Normal-incidence high-temperature, mid-infrared, InAs/GaAs vertical quantum-dot infrared photodetector', *IEEE. J. Quant. Electron.* **37**, 1412–1419.

Stiff-Roberts, A. D., Krishna, S., Bhattacharya, P. & Kennerly, S. W. (2002), 'Low bias, high temperature performance of a normal-incidence InAs-GaAs vertical quantum-dot infrared photodetector with a current blocking layer', *J. Vacc. Sci. Tech. B* **20**(3), 1185–1187.

Tang, S.-F., Lin, S.-Y. & Lee, S.-C. (2001), 'Near-room-temperature operation of an InAs/GaAs quantum-dot infrared photodetector', *Appl. Phys. Lett.* **78**(17), 2428–2430.

Tersoff, J. & LeGoues, F. K. (1994), 'Competing strain relaxation mechanisms in strained layers', *Phys. Rev. Lett.* **72**(22), 3570–3573.

Towe, E. & Pan, D. (2000), 'Semiconductor quantum-dot nanostructures: Their application in a new class of infrared photodetectors', *IEEE J. Quant. Electron.* **6**(3), 408–421.

Xu, S. J., Chu, S. J., Mei, T., Wang, X. C., Zhang, X. H., Karunasiri, G., Fan, W. J., Wang, C. H., Jiang, J., Wang, S. & Xie, X. G. (1998), 'Characteristics of InGaAs quantum dot infrared photodetectors', *App. Phys. Lett.* **73**(21), 3153–3155.

Ye, Z., Campbell, J. C., Chen, Z., Kim, E. T. & Madhukar, A. (2002), 'Normal-incidence InAs self-assembled quantum-dot infrared photodetectors with a high detectivity', *IEEE J. Quant. Electron.* **38**(9), 1234–1236.

Appendix A

Automated Photocurrent & Noise Current Measurement and Data Acquisition Using LabView

A.1 Introduction to LabView

LabView is a graphical programming environment for designing test, measurement, and control systems. LabView programs and components are called virtual instruments (VI). VIs are created using a visual programming language, where one wires together different command blocks to create program loops and functions. For each VI, there is a corresponding graphical interface, called the front panel, where inputs and buttons relating to controls and variables within the code are placed. One can use VIs to interface different electronic devices, over different interfaces such as GPIB, and then pass data between them. The great benefit of LabView over traditional programming systems is the ability to visually follow the flow of real signals through the program, and the exhaustive list of standardised commands and driver modules to communicate with electronics. LabView programs are capable of anything from simple temperature monitoring to automating experimental measurement, data acquisition, and data analysis.

A.2 Program Overview

The program detailed here was created to automate a laborious combined photocurrent and noise measurement, storing the data on computer afterwards. This measurement is described in detail in chapter 3. This program controls two devices within the noise and photocurrent measurement experiment (in figure 3.8), an SRS-570 low noise current preamplifier, and an SRS-760 FFT spectrum analyser. The measurement is a voltage sweep applied to a QDIP set up to receive a signal from a modulated black body source. As the voltage is changed, the signal strength and noise level are recorded, along with the voltage and sensitivity settings.

A.2.1 The Front Panel

Figure A.1 shows the labview front panel interface for the noise measurement program. On the left, it takes a full set of inputs for the SRS-570 low-noise current preamplifier. The list of inputs is exhaustive, since the current amplifier is a 'listen-only' device designed to use an RS-232 serial interface. As such it is not capable of sending any signals when the amplifier input is overloaded, and must be 'told' when to make sensitivity changes. This hardware limitation means that before measurement, it is necessary to set up a test device in the system. The user must run a quick manual bias sweep to the test device using the current amplifier and a multimeter (for voltage readings), taking note of the bias values for which the device is overloaded. Otherwise, the default values can be accepted, but they may not be suitable for all devices undergoing measurement. If the input signal level is too high for the current amplifier's current sensitivity, the amplifier will show an overload warning and may shutdown its input port, requiring a reboot of the amplifier.

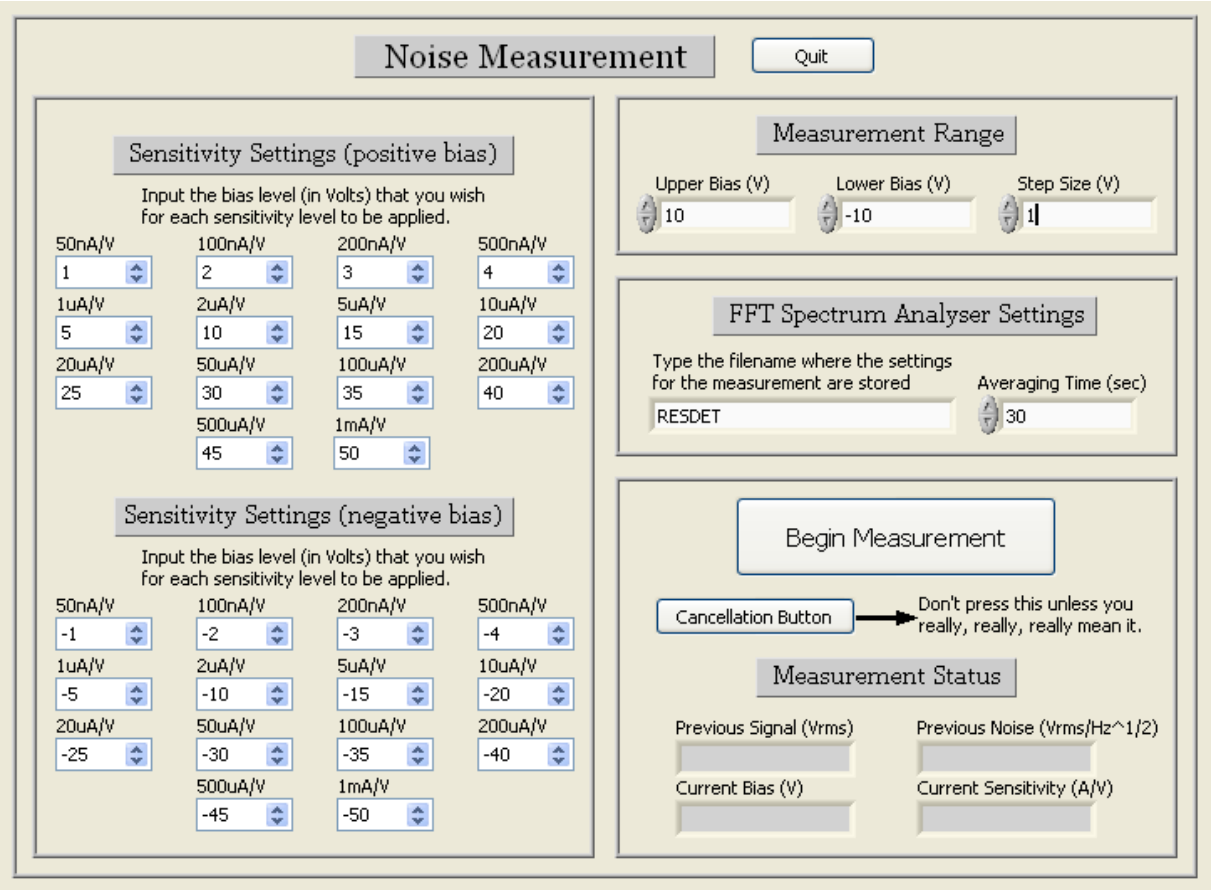

Figure A.1: Noise measurement program front panel, showing the input parameters and the status read-outs.

The right of the panel has the measurement bias voltage range and step size at the top. Beneath this is the input for the filename for the signal analyser pre-sets, and the input

for the amount of time the user wishes to allocate for each step in the measurement. The signal analyser pre-sets file contains all of the measurement parameters, such as the bandwidth, central frequency, averaging method, etc. This file is created using the signal analyser, with which it and can be altered and saved, enabling the control of the measurement parameters, without having the signal analyser's user interface and controls replicated within the LabView program. The lower-right quarter of the panel contains the status readouts as well as the start and stop buttons to begin or cancel a measurement, respectively. If the cancellation button is pressed, the current measurement step will continue for however long there is remaining in the averaging time, after which the process will be aborted.

A.2.2 Initialisation

Once all of the settings have been input, and the measurement button pressed, the program follows a simple loop, first carrying out the required device initialisation in figure A.2. The initialisation is a simple example of Labview programming, showing two instructions carried out simultaneously. The uppermost instructions are a series of GPIB commands contained within a linear sequential case statement, flowing in order of left to right. In all cases the commands are simple strings, denoted by their pink wiring, that are concatenated together before being sent to the electronic devices. Note the square block with the pink outline & grey colouring on the far left of the signal analyser initialisation. This is a generic control symbol, where the data stored in it is linked to the program front panel, which in this case is the filename input box.

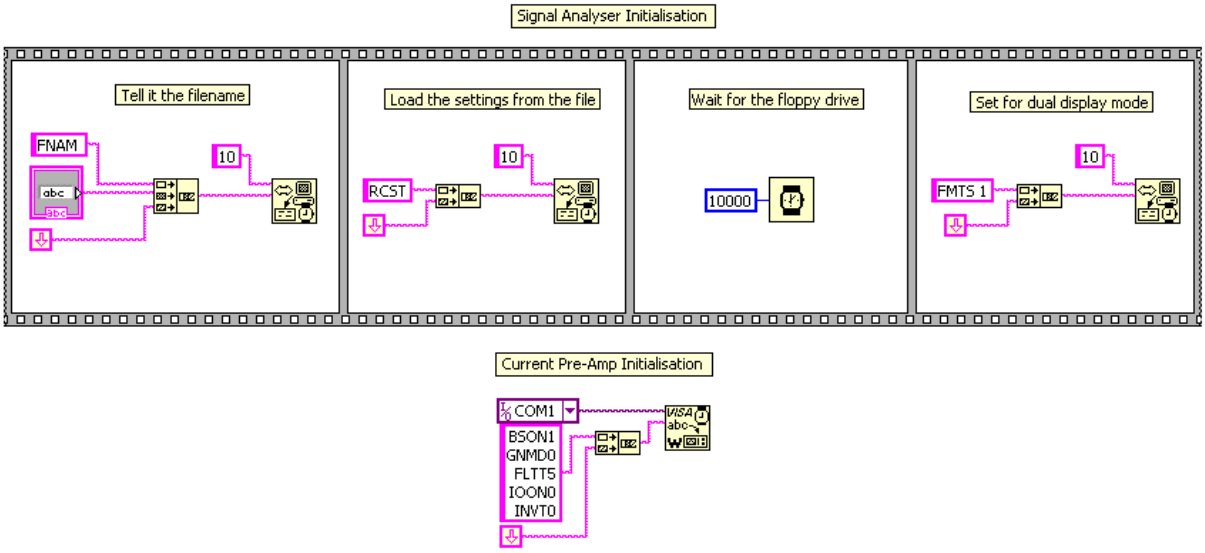

Figure A.2: Program initialisation, showing the two device initialisation command sets carried out simultaneously.

These initialisation instructions simply command the FFT spectrum analyser to load the set of user-defined settings from the floppy drive built into itself, and apply the settings to set itself up for the measurement. Below the spectrum analyser initialisation commands are the instructions for the current amplifier. These are simply a set of device dependent commands sent from the computer's COM port to the RS-232 interface on the preamplifier. The amplifier is set to accept remote instructions, and the correct bias and filter modes are set.

A.2.3 Main Execution

Once the initialisation has been carried out, the main program loop is executed. The first instructions deal with the bias and the measurement sensitivity and are shown in figure A.3. The bias is calculated as a simple linear ramp starting from the maximum value given by the user and stepping downwards, with each value determined by the current program iteration number. This bias value is then applied to the amplifier and also stored in an array data structure. The sensitivity value that is sent to the amplifier is determined by taking the bias value as an input into a series of 'if' statements. These statements compare the current bias with the bias ranges that have been specified for various sensitivities by the user on the front panel. The desired sensitivity is then saved in the data array and sent to the current amplifier.

The next stage of execution is to command the spectrum analyser to begin measurement (figure A.4). After this there is a time allocated by the user for the measurement to finish (figure A.5). Even though each measurement is actually an average of 50 or so scans made by the spectrum analyser, it only takes a small amount of time to complete, unless the user has overestimated the wait time. Immediately after are commands to pause the analyser's scanning to finish the averaging, and to check the cancellation button's status.

Finally, in figure A.6 we have the commands to acquire the data from the spectrum analyser. While the analyser is paused, the finished average measurement is recorded by the LabView program. The analyser must first be sent a request to read the data from its memory stack, followed by a read command which then sends the photocurrent data point to the data array on the PC. The same procedure is used immediately afterwards to acquire the noise current data point. The signal analyser is then un-paused, readying it for the next measurement in the bias sweep.

Once the program has run for its full voltage sweep, the finished array of data is formatted and written to a text file. The user is then presented with a "Save As" dialogue box so they can choose the files' name and save location. After the user has chosen where the data will be saved and input the filename, the data is saved and the program finishes execution, returning to its initial state.

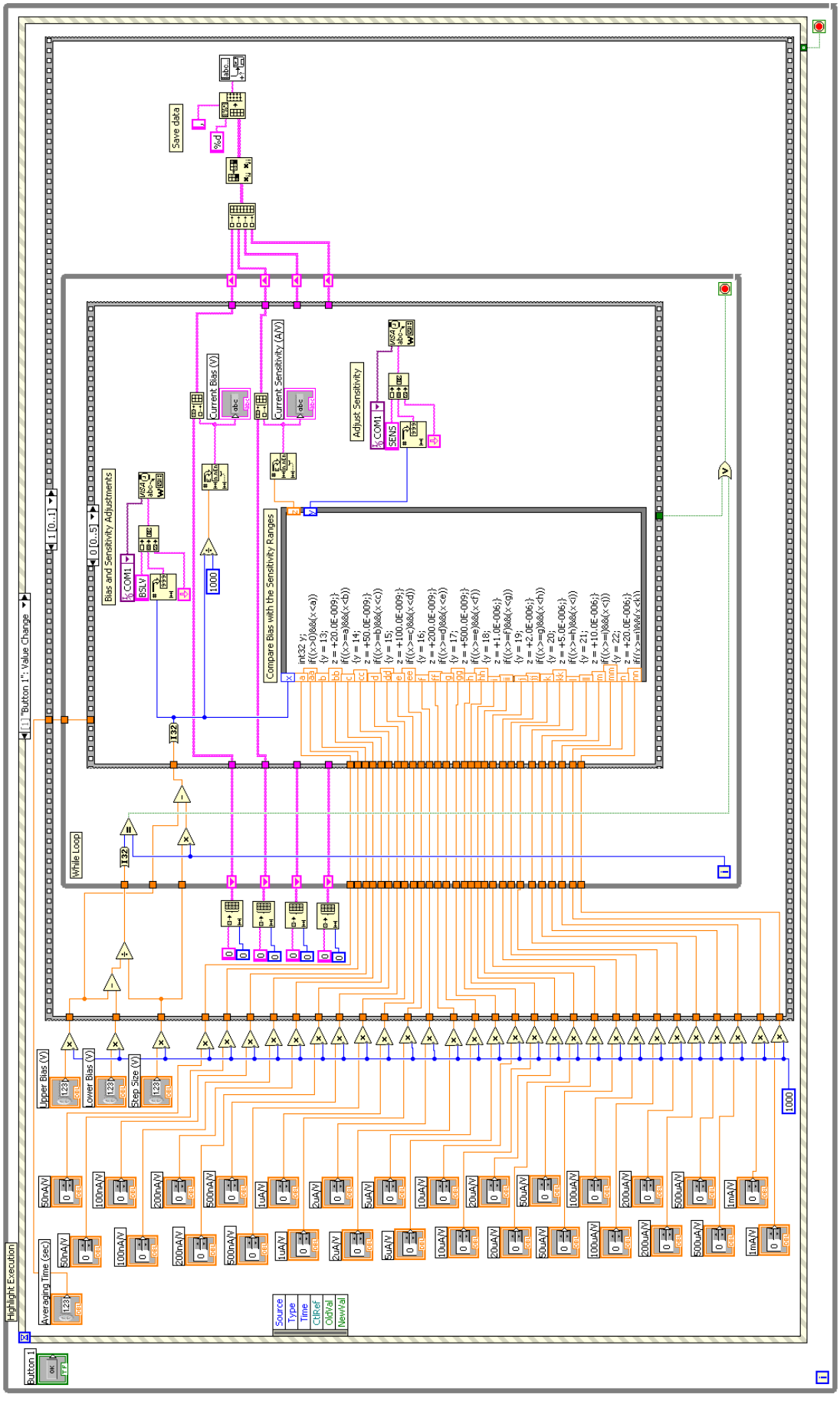

Figure A.3: Main program wiring. This sets the bias on the QDIP and the sensitivity on the current amplifier, before saving those values to the data array.

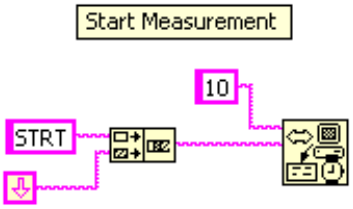

Figure A.4: Starting the signal analyser measurement. The device command (STRT) is concatenated with a line feed and sent to the FFT signal analyser identified by the device number 10 using the GPIB interface. All the communications with the signal analyser and current amplifier in the program follow a similar format.

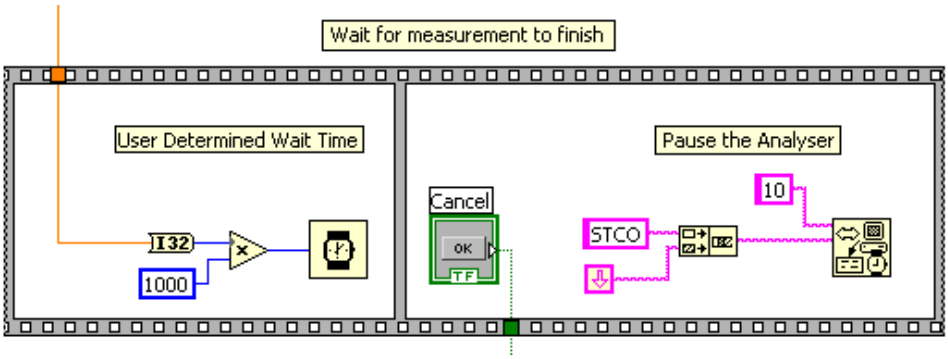

Figure A.5: Waiting for the measurement to finish. The program waits for the time defined by the user, then pauses the signal analyser and checks the status of the cancellation button.

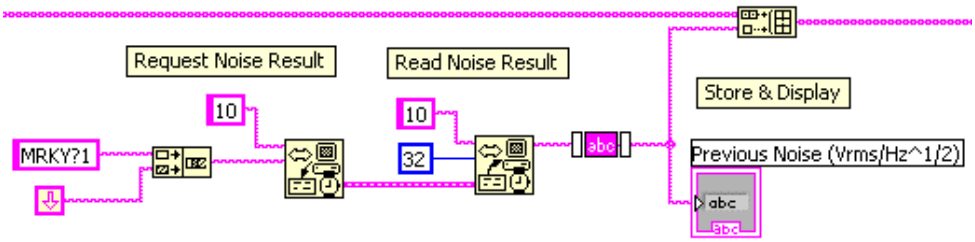

Figure A.6: Acquiring a noise current data point and storing it in the data array. While the analyser is paused, a data request is sent to the device, followed by a data read command. The acquired data is passed to the display as well as the array that stores the accumulated data in LabView.